Experimental flow studies in a city neighborhood

M.A. Mejia Morales

▶ **To cite this version:**

M.A. Mejia Morales. Experimental flow studies in a city neighborhood. Environmental Sciences. 2018. hal-02607834

HAL Id: hal-02607834
https://hal.inrae.fr/hal-02607834v1

Submitted on 16 May 2020

HAL is a multi-disciplinary open access archive for the deposit and dissemination of scientific research documents, whether they are published or not. The documents may come from teaching and research institutions in France or abroad, or from public or private research centers.

L'archive ouverte pluridisciplinaire **HAL**, est destinée au dépôt et à la diffusion de documents scientifiques de niveau recherche, publiés ou non, émanant des établissements d'enseignement et de recherche français ou étrangers, des laboratoires publics ou privés.

Internship Report

INTERNATIONAL MASTER IN HYDRAULIC AND CIVIL ENGINEERING

Academic Year 2017 - 2018

EXPERIMENTAL FLOW STUDIES IN A CITY NEIGHBOURHOOD

IRSTEA, centre de Lyon-Villeurbanne

Tutors: André PAQUIER, Sébastien PROUST, Fabien THOLLET, and Emmanuel MIGNOT

School Tutor: Philippe SECHET

Project Graduation, MASTER 2

Miguel Angel MEJÍA MORALES

NON-CONFIDENTIAL

Abstract

During the internship, experiments were conducted in a hydraulic model called MURI, located in the Hydraulics and Hydromorphology Laboratory of Irstea, Lyon-Villeurbanne. The model consists of a tilting platform 5.4 m long and 3.8 m wide, with 3 longitudinal and 3 transversal streets of 15 cm in width, formed by horizontal PVC plates and transparent plastic walls that represent the buildings of a neighborhood.

In a first stage, tests were carried out to know the physical and hydraulic characteristics of the model, as well as the performance of the different measuring instruments available. An Acoustic Doppler Velocimeter was used to measure the flow velocities and an Ultrasonic Distance Sensor for the flow depths.

The second stage consisted of measuring water depths, flow velocities and turbulence parameters for two different geometrical configurations, the first one using a longitudinal street and isolating it from the others in order to obtain a straight flume, and the second one moving the plates that isolated the street at one of the crossroads to obtain lateral cavities in the straight flume.

In the first configuration a uniform regime was established with the help of a downstream control section, setting a flow rate of 3 l/s, vertical distributions of the flow velocity were obtained, as well as cross-sectional velocity and velocity fluctuation distributions in order to identify secondary currents.

For the second configuration, the same flow rate and slope conditions were maintained, and the same tests were performed as in the previous configuration. In the area of the cavities, velocity measurements were made, the spanwise gradient of streamwise velocity was obtained, and the location of the mixing layers was observed in reference with the interface between cavities and the main flow.

Acknowledgements

To **André Paquier** for giving me the opportunity to collaborate on this internship, for his time and advice on this report.

To **Sébastien Proust**, for his guidance, his support, and because his advice motivated me to complete this internship and continue on the path of research.

To **Fabien Thollet**, for his patience in teaching me how to use the model, and for helping me to solve the various problems that arose during the experiments.

To **Emmanuel Mignot**, for his comments, his advice and his willingness to explain to me about the various topics.

To **Marc Chatelain**, for his help and advice for the tests.

To **Alexis Buffet**, for his help in carrying out the tests and solving the problems with the model.

To **Gaël Combe**, for his support and confidence in the realization of this master's degree.

To **CONACYT** and **Alianza FiiDEM**, for their monetary support throughout these two years to complete the master's degree.

To my **grandparents**, for all their affection and for always having me in their minds.

To my parents, **Vicente** and **Beatriz**, and my sister **Angélica**, for all their support during these two years, for all their love and understanding, for teaching me to chase my dreams, and above all for never leaving me alone.

To my girlfriend, **Rocío**, for her patience, for her sacrifice, for her dedication, for teaching me that distance is no reason to let things go. Thank you for your support, for your happiness, for walking with me on this adventure, and especially, thank you for your love, because despite the distance I never felt alone.

Notation

b	Width of the channel (street)
d	Flow depth
k_s	Equivalent sand roughness
Q	Flow rate
Q_{in}	Inlet flow rate
Q_{out}	Outlet flow rate
S_0	Slope of the channel bed
S_f	Slope of the energy grade line
S_w	Slope of the water surface
U_b	Bulk velocity ($=Q/bd$)
u_x, u_y, u_z	Instantaneous streamwise, spanwise, and vertical velocities
U_x, U_y, U_z	Time-averaged streamwise, spanwise, and vertical velocities
$u_x^{'}$, $u_y^{'}$, $u_z^{'}$	Fluctuations of the streamwise, spanwise, and vertical velocities
x	Streamwise direction
y	Spanwise direction
z	Vertical direction
Z	Water surface elevation
$< .. >_x$	Spatial averaging along x-direction
$< .. >_y$	Spatial averaging along y-direction
$< .. >_{x,y}$	Spatial averaging in the horizontal plane
$< .. >_{y,z}$	Spatial averaging in the transverse plane
μ	The mean of the data set
σ	The standard deviation of the data set

Contents

Chapter 1

Introduction

1.1 About the project

1.1.1 General context

Urban flooding is one of the most frequent natural disasters today, either because of changing climatic conditions in recent years or because of poorly planned urban settlements that invade runoff areas. There are many studies and research on floods, however, most of them are large-scale, and it is not possible to take into consideration the different types of existing construction, such as buildings, parks, houses, etc.

Since this type of event is one of the most important natural hazards, it is of vital importance to have studies on a local scale that allow us to characterize and quantify in some way the flood hazard and associated risk according to the type of buildings.

In this context, the National Research Institute of Science and Technology for Environment and Agriculture (IRSTEA) has acquired a physical scale model representing a district of a city to carry out different experiments and study urban flooding.

In this model, which is of recent acquisition, it is necessary to perform several tests to know its characteristics, as well as the characteristics of the measurement instruments available to be used on it.

1.1.2 Objective

The main objective is to obtain information about the hydraulic and physical characteristics of the model, to carry out experiments that allow to observe the behaviour of the model under certain configurations and from there to make corrections if necessary and issue recommendations for its use in future experiments.

1.1.3 Work team

The work team consists mainly of two researchers from Irstea, one researcher from the Laboratory of Fluid Mechanics and Acoustics (LMFA), and two technicians from Irstea. The researchers lead this internship with their observations, experience and theoretical knowledge, and the two technicians provide their experience and technical knowledge to enable experimentation on the physical model.

1.2 Irstea

It is a research organization which, since more than 30 years, works on major issues of a responsible agriculture and territories sustainable planning, water management and related risks,

drought, floods, inundations, the biodiversity and complex ecosystems study in their interrelation with human activities. It is a Public Scientific and Technological Institution, which is under the double supervision of the Ministries of Research and Agriculture.

1.2.1 Brief history

On 20th May 1955, a legislative decree created the CNEEMA as the "National Centre for Studies and Experiments on Agricultural Machinery" bringing together the central and regional stations, the Experimental Hydraulic Station, the Secretariat for the Agricultural Machinery Management Committee and the Department of Documentation on Agricultural Machinery. Originally, CNEEMA employed 40 people. In 1970, it had 230 employees, one third from the Ministry for Agriculture and the rest contractual agents.

FIGURE 1.1. Institute's logo.

In parallel, the Agriculture Administration came up against precise technical problems within the framework of its assignments and had to rely on specialized services to exert its responsibilities. Following the reform of the Departments outside the Ministry for Agriculture a scientific organisation was created: CERAFER (National Centre for Technical Studies and Technological Research for Agriculture, Forests and Rural Equipment). In 1972, this centre became the CTGREF (Technical Centre for Rural Engineering of Water and Forests) with the aim of essentially focusing its activities on information and technical support for the Ministry of Agriculture's central services.

On 21st January 1981, CNEEMA and CTGREF merged to create CEMAGREF and in 1985 it took on the status of a scientific and technical public establishment (EPST) supervised by both the Ministry of Research and Agriculture. This change in status was completed in 1992, with the appointment of tenured or permanent staff.

The CEMAGREF becomes IRSTEA in November 2011, to coincide its name with the current reality of his research, which has evolved over the years from problems of mechanization and rural development to agro-environmental issues.

1.2.2 Nowadays

Irstea has 1533 partners and contacts, including 1129 scientists, engineers, PhD students and doctors. Working in 9 regional centres (figure1.2), Irstea researchers are in direct contact with the various local areas, and their field observations form the basis of their research, the research is divided into three departments: water, eco-technologies and land.

- Water Department: Almost half of Irstea's research work is deployed in studying and managing surface water and any associated activities. The institute runs a wide range of activities dedicated to water resources, aquatic environments, infrastructures and uses.

- Environmental Technologies Department: The fields of application of this department's research concern the agro-industrial sectors: agriculture and agri-food, waste management and storage, purification and new technologies.

- Land Use Department: This department follows multidisciplinary approaches combining ecology, remote detection and human sciences are particularly adapted to study this sustainable development process and tackle the territory in its different dimensions.

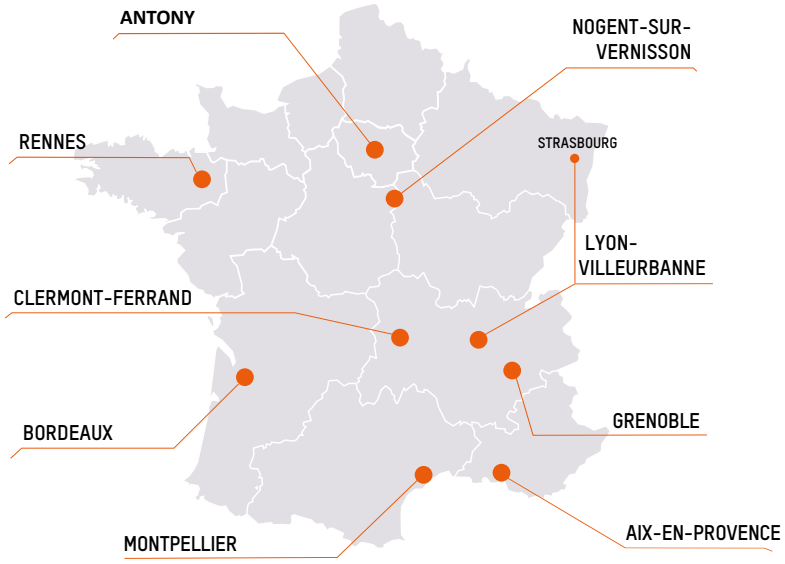

FIGURE 1.2. The research centres of IRSTEA.

1.2.3 Lyon-Villeurbanne Centre

Lyon's major knowledge production goals involve improving water resource management, reducing pollutant and toxic waste impact on aquatic ecosystems, reducing vulnerability to risks associated with the water cycle, flooding and also droughts. The Lyon-Villeurbanne Centre comprises three research units, including one relocated to Strasbourg.

- RiverLy: It is a multidisciplinary unit whose objective is to understand the functioning of watercourses, also supports the management of water resources and biodiversity in hydrosystems in the context of global change.
- REVERSAAL: It conducts research on urban effluent recovery and treatment processes: wastewater, urban rainfall discharge, and sewage sludge.
- GESTE: It is an interdisciplinary unit in social sciences that produces knowledge, methods and expertise to support collective action in the field of territorial environmental management.

The topic of this internship was proposed by the River Hydraulics division, which belongs to the RiverLy research unit.

1.3 Experimental model

1.3.1 Model components and characteristics

The Urban Model for the Study of Flood Risk, *MURI* (Maquette Urbaine pour étudier les Risques d'Inondation) consists of an adaptable city model with a 3.8 m x 5.4 m rectangular platform to study urban flooding processes. It is composed of three floors; in the first one is where a pipe network is located, these pipes simulate the operation of a sewage network. This network is composed of a main collector oriented longitudinally, with a diameter of 100 mm, and secondary pipes of 50 mm in diameter, parallel and perpendicular to the collector.

In the second one there is an arrangement of 3 longitudinal and 3 transversal streets, the streets are delimited by vertical transparent walls of plastic type PETG of 150 mm high fixed to a horizontal slab formed by non-transparent PVC plates [15], and in the third one there is

the measuring gantry built by aluminium beams, which allows the movement of the measuring devices in longitudinal direction (x-axis), transversal direction (y-axis) and height (z-axis).

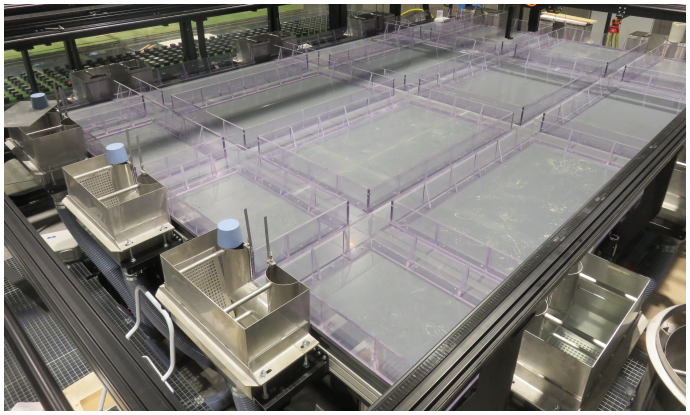

FIGURE 1.3. MURI, view of the streets.

The streets represented in the model have a width of 150 mm, at the end of each street there is a tank that serves for the supply or evacuation of water, in the case of longitudinal streets, at one end there are the water supply tanks (upstream side) and at the other end the drainage tanks (downstream side). In the case of transversal streets, the tanks can be used to supply or drain water, at these ends we will call them right and left sides, see figure 1.4.

FIGURE 1.4. Plan view of the street arrangement in MURI.

Chapter 2

Theoretical Aspects

2.1 Types and state of the flow

The flow in the streets of MURI will be analyzed as open-channels flow, and the most usual classification is as follows:

- *Steady and Unsteady flow.* Time is the criterion, and it is *steady* when the water depth is constant during the interval of time $\frac{\mathrm{d}d}{\mathrm{d}t} = 0$, otherwise it is *usteady* $\frac{\mathrm{d}d}{\mathrm{d}t} \neq 0$.
- *Uniform and Varied flow.* Space is the criterion, and it is *uniform* if the water depth is the same along the reach under study $\frac{\mathrm{d}d}{\mathrm{d}x} = 0$, otherwise it is *varied* $\frac{\mathrm{d}d}{\mathrm{d}x} \neq 0$.

The state of the flow is governed by the effects of viscosity and gravity relative to the inertial forces of the flow,

- *Viscosity.* Depending on the ratio of inertia to viscosity, the flow may be laminar, turbulent, or transitional. This effect can be represented by a dimensionless parameter known as the *Reynolds number*, defined as:

$$\mathbf{R} = \frac{4R_h u}{\nu} \tag{2.1}$$

  Where u is the flow velocity, R_h is the hydraulic radius, and ν is the kinematic viscosity of water, which is 1×10^{-6} m^2/s at 20 °C.

$\mathbf{R} < 500$	laminar flow
$500 \leq \mathbf{R} \leq 12500$	transitional flow
$12500 < \mathbf{R}$	turbulent flow

  In a *laminar flow* the viscous forces are so strong relative to the inertial forces that the flow is governed by viscous forces; here the water particles appear to move in definite smooth paths. In a *turbulent flow* the inertial forces are so strong relative to the viscous forces, so, the flow is governed by inertial forces; the water particles move in irregular paths. Between these two states, there is the *transitional flow.*

- *Gravity.* Depending on the ratio of inertia and gravity, the flow may be subcritical, critical, o supercritical. This classification is based on a dimensionless parameter known as the *Froude number*, defined as,

$$\mathbf{F} = \frac{u}{\sqrt{gD}} \tag{2.2}$$

  Were u is the flow velocity, D is the hydraulic depth, and g the acceleration of gravity.

$\mathbf{F} < 1$ subcritical state
$\mathbf{F} = 1$ critical state
$\mathbf{F} > 1$ supercritical state

The dominator in Eq. 2.2 is the celerity of the small gravity waves in shallow water. When the flow is *subcritical*, the flow velocity is smaller than the celerity of these waves, therefore, such waves can propagate upstream. When the flow is *supercritical*, the flow velocity is grater than the celerity, and the waves cannot propagate upstream against the flow.

2.2 Uniform Flow

2.2.1 Setting uniform flow

The uniform flow has the following main features:

- Depth, flow area, flow velocity and discharge at every section of the reach are constant.
- The energy line, water surface and reach bottom are all parallel; $S_f = S_w = S_0$.

A uniform flow will be established if the resistance is balanced by the gravity forces.

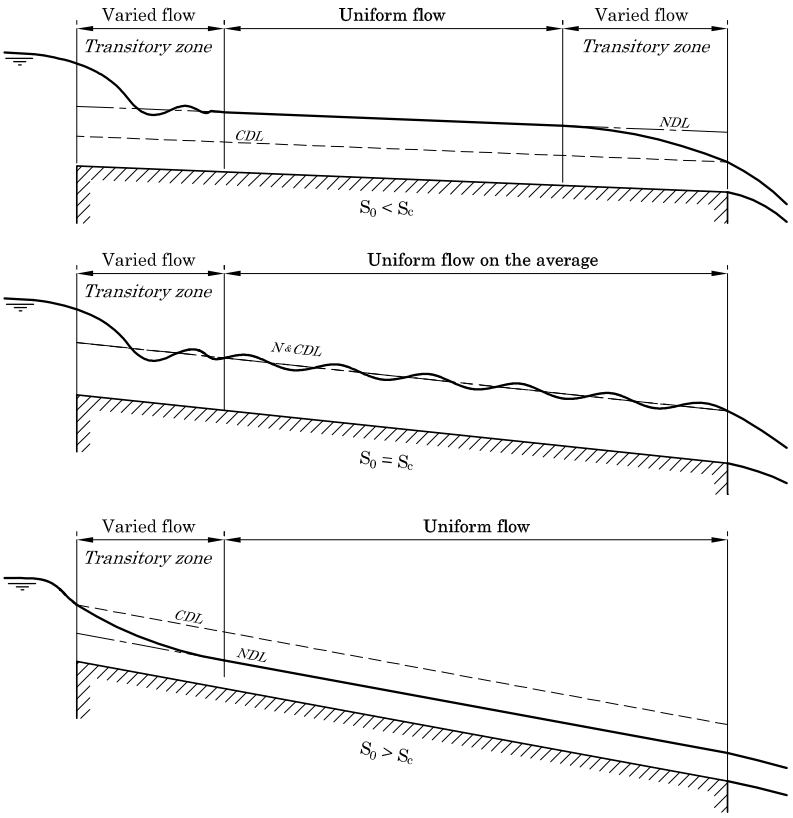

FIGURE 2.1. Setting a uniform flow in a channel. *NDL* is the normal depth line and *CDL* the crtical depth line.

When the water enters the channel, the velocity and resistance are small, they will gradually increase until a balance between resistance and gravity forces is reached, and then the uniform flow is established. The upstream reach necessary to establish it is called *transitory zone* [4], and if the channel is not longer than this reach, the uniform flow can not be observed.

Strictly uniform flow is difficult to achieve, even in prismatic channels there are physical and hydraulic realities that make it almost impossible, however, this concept is the starting point for describing flow resistance relations for open channels. In general, if the deviations are not too great, the flow is *quasi-uniform*, and the basic features of uniform flow will be assumed to apply [6].

2.2.2 Basic equation

Several expressions have been developed over time, derived from the definition of uniform flow, where there is no acceleration because the forces that tend to generate motion are equal to the forces that tend to resist motion, $F_D = F_R$.

The best known and used expressions are those developed by Chézy in 1769 and Mannig in 1889. The Chezy's equation is as follows,

$$u = C\sqrt{R_h S} \tag{2.3}$$

Were u is the flow velocity, S the slope, and C is a resistance coefficient, called Chézy's C.

Mannig's equation has a similar form,

$$u = \frac{1}{n} R_h^{2/3} \sqrt{S} \tag{2.4}$$

Were n is the coefficient of roughness, known as Manning's n.

The difficulty in using these coefficients, n and C is to accurately estimate their value. In general it depends on the type of flow (Reynolds number), the boundary roughness and the shape of the channel cross section.

2.3 Gradually Varied Flow

It is the steady flow whose depth varies gradually along the length of the channel. For this flow there is some assumptions,

- The uniform flow resistance equation applies.
- The pressure distribution is hydrostatic.
- The energy equation applies.

This flow is governed by [7],

$$\frac{\mathrm{d}d}{\mathrm{d}x} = \frac{S_0 - S_f}{1 - \mathbf{F}^2} \tag{2.5}$$

Where $\frac{\mathrm{d}d}{\mathrm{d}x}$, represents the variation in water depth, d, in the flow direction.

For a specific discharge, Q, and channel conditions, the normal-depth and critical-depth lines divide the channel into three zones in the vertical dimension, see figure 2.2.

- Zone 1. Above the upper line.
- Zone 2. Between the two lines.
- Zone 3. Below the lower line.

In addition to these three zones, it is possible to classify the flow profiles according to the slope of the channel floor, this may be adverse ($S_0 < 0$), **A**, horizontal ($S_0 = 0$), **H**, critical (when it produces a critical state, $S_0 = S_c$), **C**, mild ($0 < S_0 < S_c$), **M**, and steep ($S_0 > S_c > 0$), **S**.

Since we know the zone where the flow surface is located, as well as the slope of the floor, it is possible to know in the numerator of the equation 2.5, how S_0 is respect to S_f, as well as in the denominator, if the Froude number is equal, greater, or less than 1. Then we can infer the sign of $\frac{\mathrm{d}d}{\mathrm{d}x}$ and with it, the behavior of the water surface profile can be predicted.

2.4 Turbulent Flow

Turbulent flow occurs in almost all geophysical flows, such as rivers, lakes, estuaries and oceans, and almost all man-made hydraulic structures, such as spillways, channels, sewers, weirs, etc., so the study of this type of flow is indispensable [11].

2.4.1 Characterizing Turbulence

For turbulence flow, the instantaneous velocity is defined in terms of a time-wise mean velocity and a turbulent fluctuation component. For a cartesian coordinates system, the instantaneous velocities are,

$$u_x = U_x + u'_x \tag{2.6}$$

$$u_y = U_y + u'_y \tag{2.7}$$

$$u_z = U_z + u'_z \tag{2.8}$$

This is commonly called the Reynolds' decomposition.

Because the nature of turbulence are approximately random, we can characterize them using statistical concepts. The time-wise mean velocity is defined as,

$$U = \frac{1}{t}\int_0^t u \,\mathrm{d}t \tag{2.9}$$

The turbulence strength, defined as the root mean square value of the velocity fluctuations,

$$\sqrt{\overline{u'^2}} = \left(\frac{1}{t}\int_0^t u'^2 \,\mathrm{d}t\right)^{1/2} \tag{2.10}$$

The covariance measures the degree to which two variables are interdependent, i.e., measures the correlation which exists between two variables. In the case of the velocity fluctuations in the xy plane,

$$\overline{u'_x u'_y} = \frac{1}{t}\int_0^t u'_x u'_y \,\mathrm{d}t \tag{2.11}$$

This terms $\overline{u'_i u'_j}$ are called *second-order correlations* [5] . This correlations are useful to compute the Reynolds shear stresses. In the case of xy plane, it is defined as,

$$\tau_{xy} = -\rho\overline{u'_x u'_y} \tag{2.12}$$

Theses stresses are developed due to turbulent fluctuations.

2.4.2 Boundary layer

When the movement of fluid is not affected by its viscosity, it can be treated as the flow of ideal fluid, however, a flow around a solid cannot be treated in such manner because of viscous friction. Nevertheless, only the region closest to the surface of this solid is affected by this friction, therefore, outside this *boundary layer* is assumed to be ideal fluid flow.

The surface of this boundary layer is classified as hydraulically smooth or rough; if the roughness elements are covered by the viscous sublayer, the boundary is hydraulically smooth, otherwise it is hydraulically rough.

The effects of roughness elements are usually classified with the shear Reynolds number, $\mathbf{R}_*$,

$\mathbf{R}_* \leq 5$	hydraulically smooth bed
$5 < \mathbf{R}_* < 70$	incompletely rough bed
$70 \leq \mathbf{R}_*$	completely rough bed

$$\mathbf{R}_* = \frac{k_s u_*}{\nu} \tag{2.13}$$

Where k_s is a length parameter that characterizes the perimeter roughness and it is called *equivalent sand roughness* or *equivalent sand grain size* ,u_* is the shear velocity defined as,

$$u_* = \sqrt{g R_h S_0} \tag{2.14}$$

Where R_h is the hydraulic radius.

When the boundary is hydraulically smooth, the roughness has no effect on the flow outside the sublayer, therefore, there is a *hydraulically smooth turbulent flow*, when the boundary is hydraulically rough, the flow outside the sublayer is affected by the roughness, and there is a *fully rough turbulent flow*.

2.4.3 Velocity distribution

In a 3-D flow, it is considered that there are two flow components, *primary flow*, in the streamwise direction, and a *secondary flow* transverse to it (spanwise and vertical directions). This secondary flow is commonly referred to as *secondary currents*.

For more than a century (Stearns [16]), several researchers have found that in open-channel flows, when the aspect ratio (b/d) is small, e. i., narrow channels, the maximum velocity occurs below the surface. This condition called the *dip phenomenon* is explained by the presence of a secondary currents according to several researchers, [8] [3] [14]. For instance, Nezu *et al.* [11] establishes that low-momentum fluids are transported by secondary motion from the near bank to the center, and high-momentum fluids are moved from the free surface towards the bed.

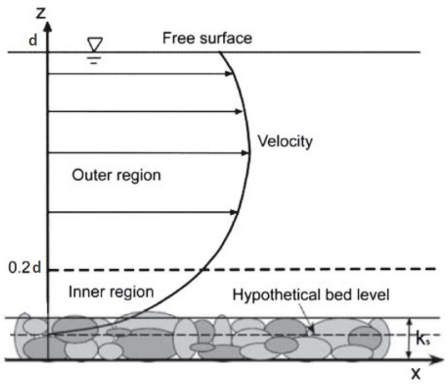

FIGURE 2.2. Vertical velocity distribution in narrow channels, [Bonakdari *et al.*, 2008].

Chapter 3

Model Characterization

3.1 Street floor levels and rail levels

To measure flow elevations in the MURI streets, there is a fixed ultrasonic sensor (US) in the measuring gantry, which measures distances or heights in this case because the measurements are made in the z axis, so to obtain the water depths in the streets is necessary to make two measurements: the distance (air height) between the floor and the sensor (h_2 in Fig. 3.1), and the air height between the water surface and the sensor.

To move the measuring instruments along the length and width of the model, the measuring gantry has longitudinal and transverse rails, and for more accurate measurements it will be necessary to check the straightness of these rails on the z-axis. To do this it will be necessary to have standing water in the streets and use the free surface of the water as a horizontal reference plane,the air height (h_1 in Fig. 3.1) between the sensor and the surface of the water will give us the necessary information to know if there are undulations in the rails that must be taken into account to correct the measurements that will be made during the experiments.

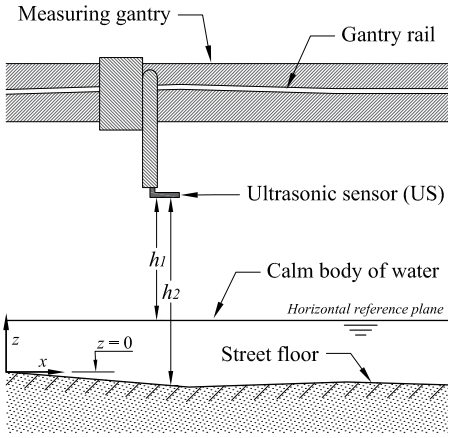

FIGURE 3.1. Diagram of the measures carried out with the US in MURI.

The measurements were made at different points along the streets, from station 300 to 5200 on the x-axis for longitudinal streets, and from station 300 to 3400 on the y-axis for transverse streets[1]. An acquisition duration for each measurement of 10 seconds at a rate of 50 Hz were chosen, and the characteristics of the mesh for taking measurements on the streets is as follow:

- $\Delta x = 100$ mm
- $\Delta y = 38$ mm

The same Δx and Δy were used for the other streets, the results obtained in the measurement of the rails are shown in figure 3.2, and a difference of 1.5 to 2 mm can be observed between the height in the initial part of the rails and the final part, with a downward slope in all cases.

The air height between the sensor and the floor was obtained in the 6 streets, these values will be useful to obtain the water flow depths for the subsequent tests, the results are shown in figure 3.3.

[1]The measurement area is limited by the size of the measurement portal, and the instruments found on it.

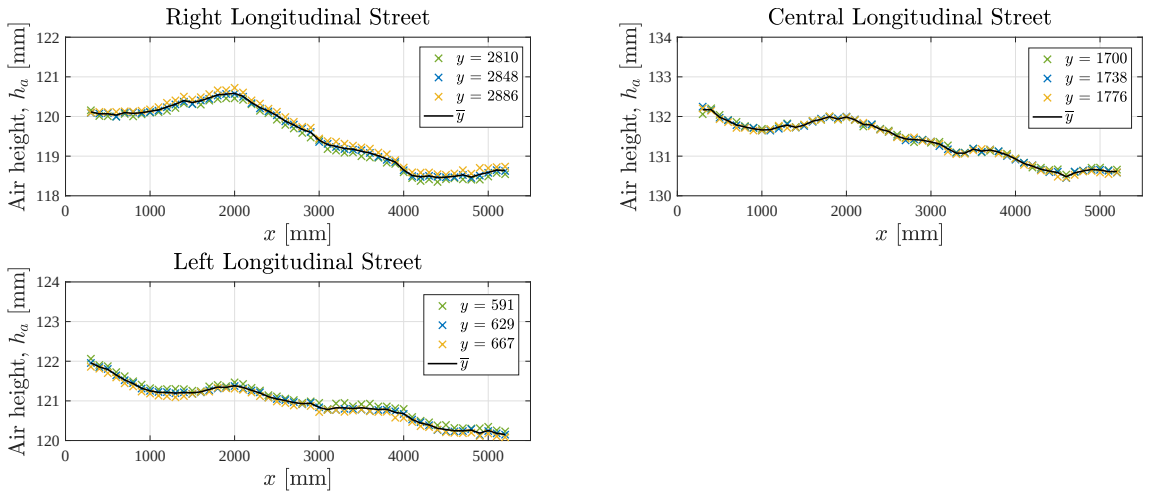

FIGURE 3.2. Measurements of the air height between the US and calm body of water, with MURI totally horizontal (the elevation of the water surface in each street at the time of the measurements was different).

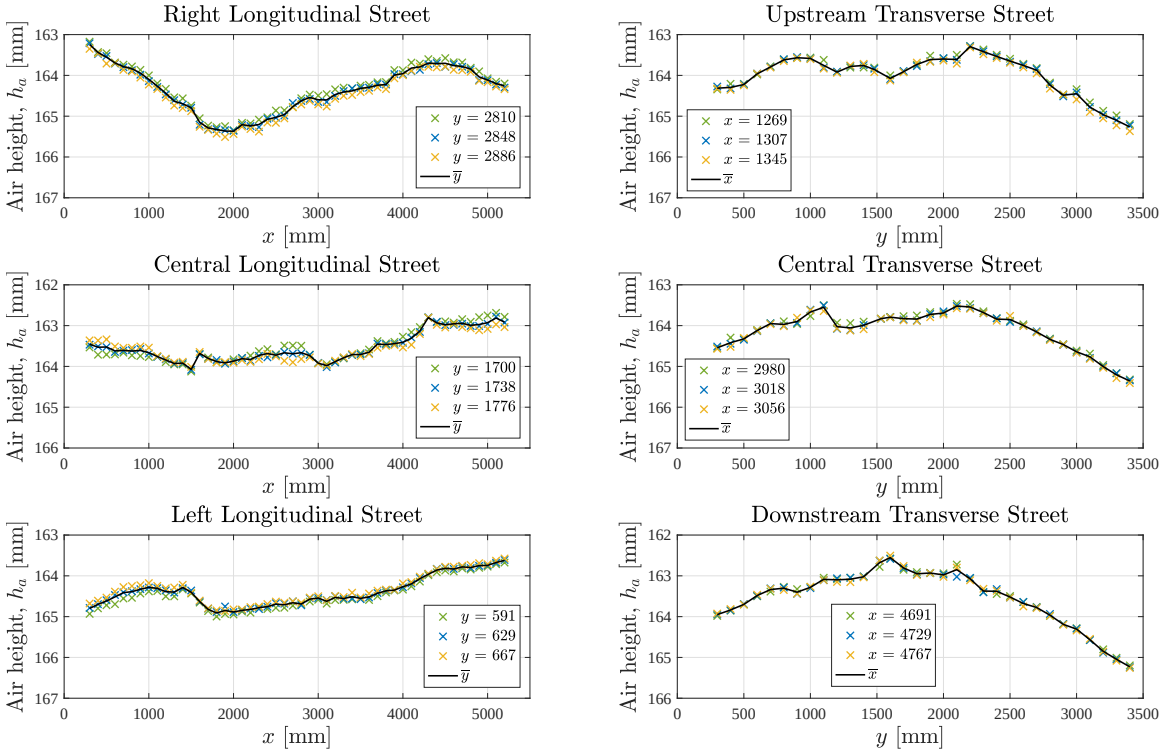

FIGURE 3.3. Levels of the streets, the vertical axis is inverted to show topography in the correct direction.

As we can see from the previous results there is a variation of the slope along all the streets, and this is explained by the fact that the floor of the streets (the PVC slab) is made up of several PVC plates, in the longitudinal sense there are 4 plates, so there are joints between each plate and apparently in some cases there is a small misalignment between the plates, and also each one has a different slope.

Figure 3.4 shows the results of the street floor levels [2], which were obtained with respect to a completely horizontal plane (standing water). These levels were calculated with the air heights obtained between the rails, the water surface, and the street floor shown in the figures above.

[2]Only the results of the longitudinal streets are shown as it is not possible to place standing water on the transverse streets at the moment due to the tests that are being carried out on the model.

To present the results, the elevation at the beginning of each street was taken as the reference elevation z=0 (see Fig. 3.1).

In addition to this and as a consequence of the results obtained, a verification of the levels on the floor of the streets was carried out with the help of a level staff and a theodolite, and then using a completely horizontal laser beam instead of the theodolite. The laser beam was used with the idea of improving the accuracy of the measurement, because the elevations in the floor of the streets has a millimetre variation, however the resolution that both the theodolite and the laser provides us is very similar, because it depends mainly on the level staff and the human eye.

The results obtained are shown in Appendix A and they are very similar to those found with the ultrasonic sensor. So it can be said that there is a variation of the slope in the streets of the model that must be taken into account to have more reliable results during the experiments.

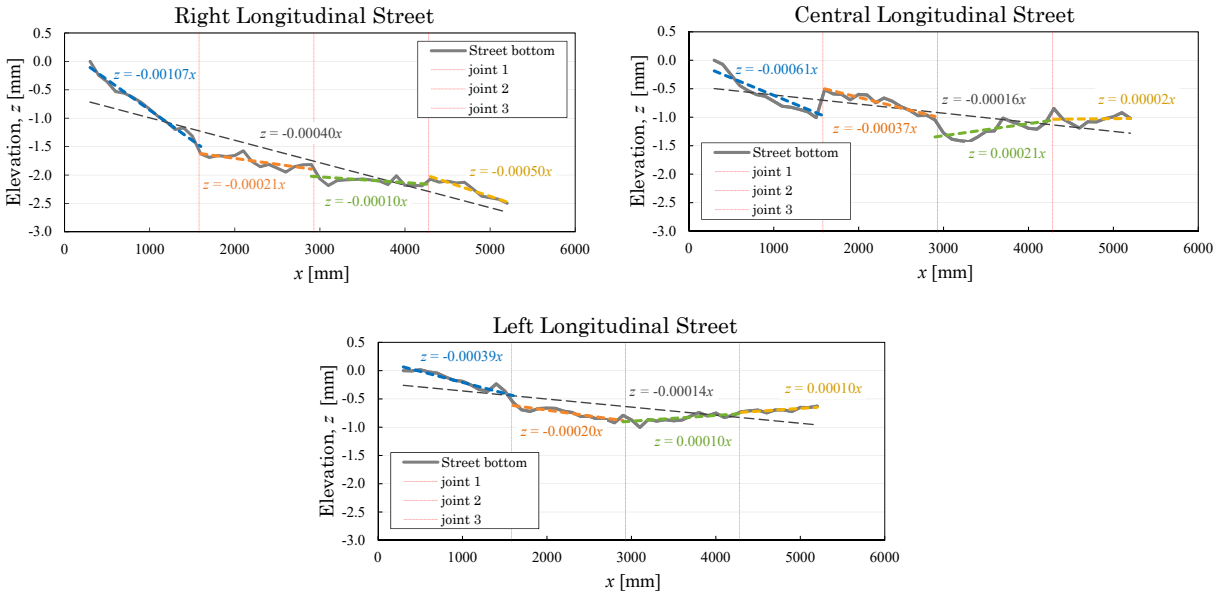

FIGURE 3.4. Floor elevations. The dashed red lines represent the location of the joints between each PVC plate, the dashed colored lines a linear regression and with it the slope in each plate.

3.2 Flow rate fluctuation

An important step is to know if the value of the flow rate is maintained over time in the model, as well as the magnitude of the fluctuations presented.

In MURI it's possible to set the flow rate value in two ways, in automatic mode and in manual mode:

- Automatic mode, the valve and flowmeter will automatically set the value of the requested flow rate for the duration of the test.
- Manual mode, the valve opening percentage is set manually, trying to establish the required flow rate, this percentage will remain fixed throughout the test.

Tests were performed for different flow rates in both modes, each test lasted 100 min, the results obtained are shown in figure 3.5. In addition, some statistical parameters were obtained to measure the tendency and dispersion of the data series of the complete samples and for periods of 20 min (the results are shown in table A.1, Appendix A).

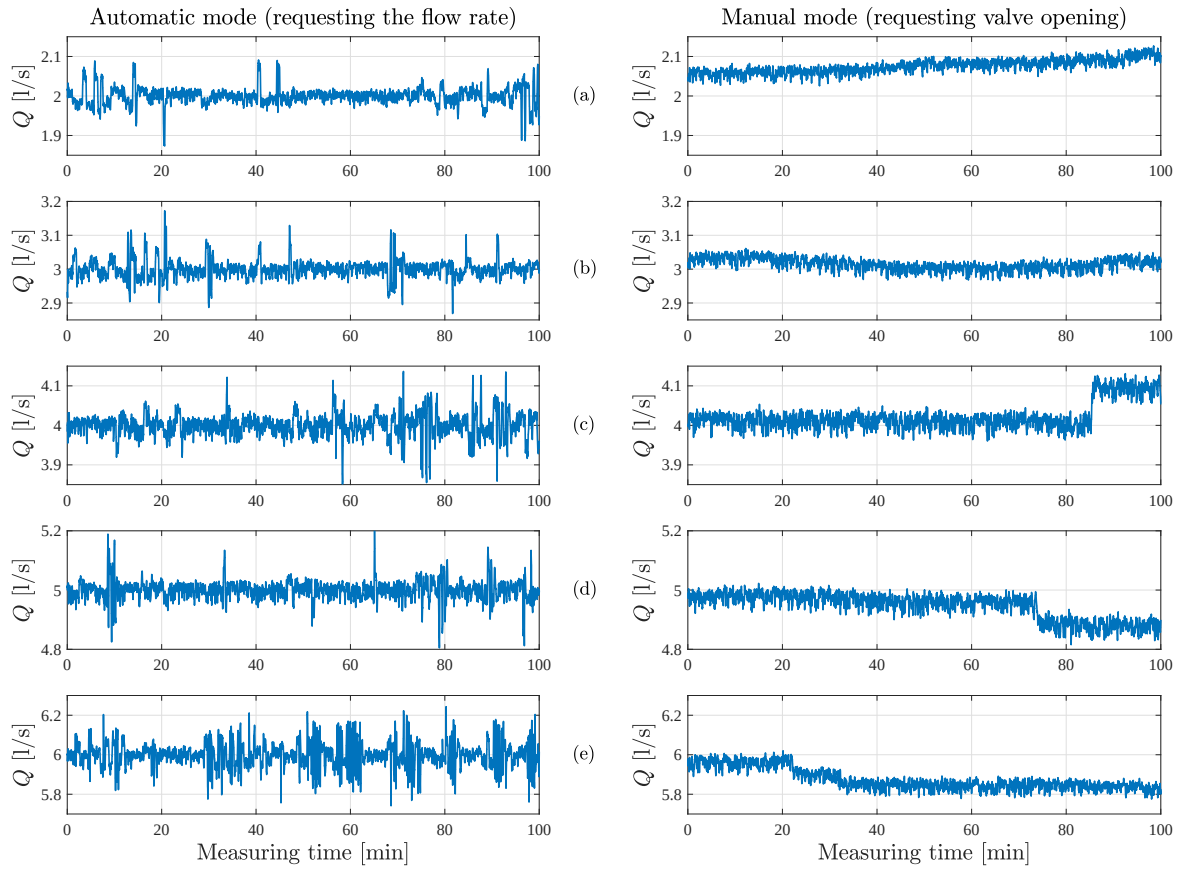

FIGURE 3.5. Flow rate evolution over time, measurements were made with a frequency of 50 [Hz]. The flow rates in [l/s] required at MURI were: a) 2, b) 3, c) 4, d) 5, e) 6.

The results show that despite having a more stable flow rate or less fluctuations using the manual mode, there is a significant problem when measurements are made over a long period of time. There is a deviation from the average flow rate because the head in the supply tank has slight variations, depending on the number of pumps used to fill this tank, as well as the models of the hydraulic hall that are in use.

As the tests to be performed will have a duration of several hours, it will be better to use the *automatic mode*, in order to avoid the observed deviations.

In the MURI's system for setting the flow rate it is also possible to change a parameter called tolerance [3], which is presented in percentage and it's by default 0.05. Some tests were carried out decreasing this value and it was observed that a value of 0.02% gives better results (see figure 3.6).

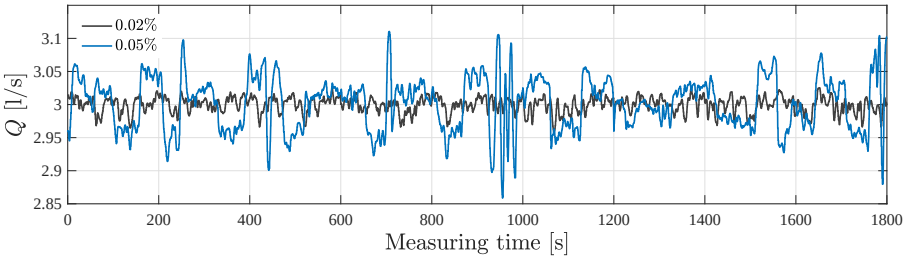

FIGURE 3.6. Flow rate evolution over time using the automatic mode for different tolerance.

Flowmeters are available at the inlet and outlet of the streets, so it is also possible to compare

[3]It is the deviation that can be tolerated with respect to the requested flow rate in the MURI system.

these two values and see the reliability of the flowmeter readings. In the following figure the results are shown.

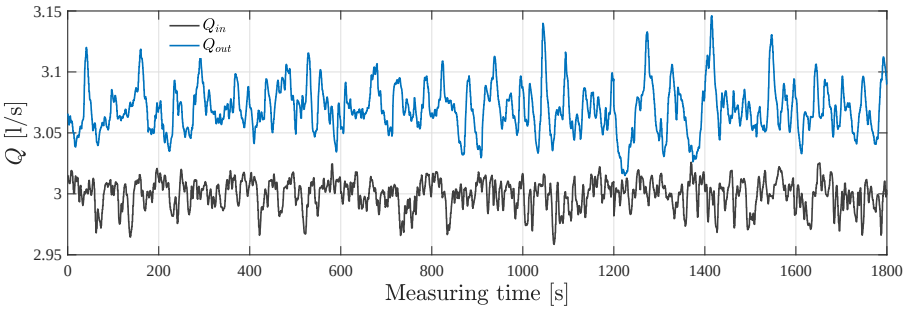

FIGURE 3.7. Flow rate evolution over time in the inlet and outlet.

It has been observed at the outlet that the flow meters record a higher value than at the inlet for the same flow rate, and this is due to the presence of air bubbles, so it will be necessary to close the valves at the outlet a little to increase the head and have the water surface before the beginning of the pipelines. This will prevent air from entering, and trapped air may be released through a valve located at the top of the pipe before the flowmeter.

3.3 Resistance coefficient estimation

To characterize the roughness of the street floor and walls in MURI, we will experimentally determine the value of k_s, which has the same limiting value of Darcy-Weisbach friction factor, f.[4]

Darcy-Weisbach friction factor, f, can be estimated by the Colebrook formula:

$$\frac{1}{\sqrt{f}} = -2\,log\left(\frac{k_s}{12R_h} + \frac{2.5}{\mathbf{R}\sqrt{f}}\right) \tag{3.1}$$

To define the k_s value, experimental water depth profiles for different discharges values will be obtained and compared with the theoretical water depth profiles. To compute the theoretical profiles the equation 2.5 of gradually varied flow will be used.

To compute the value of S_f, the Manning equation will be used, however the coefficient n, will be put in terms of f,

$$S_f = \frac{f}{4R_h}\frac{u^2}{2g} \tag{3.2}$$

The method used to compute the theoretical profiles consists of carrying out the calculations by steps from station to station where the hydraulic characteristics have been determined. In such case the distance between stations and the flow depth in the first station are given and the procedure is to determine the flow depth at the following stations.

All the profiles were reproduced in subcritical regime and the different slopes of the floor found in the previous section were used. The flow depth at which each theoretical profile will be started is the most downstream flow depth found in each experimental profile.

To compare the profiles it's necessary to know how well the theoretical one fits the experimental one, and to check it the Mean Square Error method (MSE) will be used. It measures the average of the squares of the deviations, which is the difference between the estimator and what is estimated, it is always non-negative and values close to zero are better.

$$MSE = \frac{1}{n}\sum_{i=1}^{n}(h_{exp} - h_{the})^2 \tag{3.3}$$

[4]Factor used to asses flow resistance in pipelines.

The experimental flow profiles were obtained on the right longitudinal street with flow rates between 2 and 6 l/s, and for each flow rate value several theoretical profiles were obtained with the geometrical characteristics of this street and with different k_s values proposed.

Each profile was compared and a curve[5] was obtained for each discharge with the MSE values and the proposed range of ks values. The table below shows the k_s values found for the smallest MSE value for each proposed flow rate.

TABLE 3.1. Sand grain size k_s values found for different discharge values.

Q [l/s]	2	3	4	5	6
k_s [m]	3.2×10^{-5}	2.5×10^{-5}	4.2×10^{-5}	3.6×10^{-5}	4.3×10^{-5}

With the values shown in table 3.1 a comparison will be made to know which is the optimal value for any flow rate.

For this purpose, a theoretical water depth profile will be computed for each flow rate (2, 3, 4, 5 and 6 l/s) using the k_s values obtained, i.e. we will have five theoretical profiles calculated with each k_s value. The theoretical profiles will be compared with their corresponding experimental profiles using the MSE method, and the value closest to zero after comparing all the calculated profiles with each k_s value will be the one that best fits and the optimal for different flow rates.

Having carried out the different calculations it can be concluded that the optimum roughness value is $k_s = 3.6 \times 10^{-5}$ m (see Fig. 3.8). This value is consistent with the values reported for thermoplastic materials in different publications, as well as the values found by Lalanne [9].

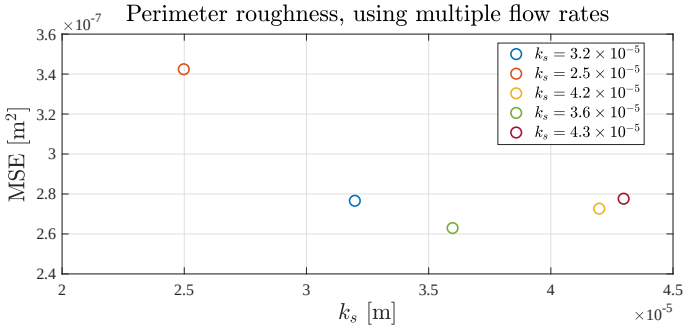

FIGURE 3.8. Comparison of the water profiles, using for the theoretical profile the k_s value that generates the best fit.

3.4 Measuring techniques

3.4.1 Water depths

The water depths have been measured using an ultrasonic distance measuring sensor, *US* (see Fig. 3.9), and according to the manufacturer, the repeat accuracy is less than 0.5 mm and the resolution less than 0.3 mm . In order to know the appropriate acquisition duration for the measurements, some convergence tests were performed using two different discharge values and measuring for 400 seconds at a rate of 50 Hz.

Four independent measurements were performed for two flow rate values, the results are shown in the figure 3.10.

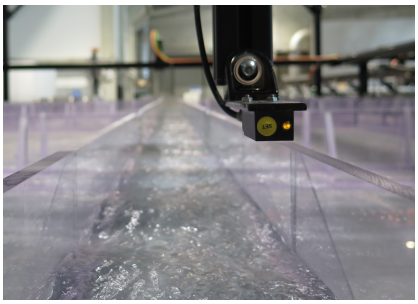

FIGURE 3.9. Ultrasonic sensor on one of MURI's streets.

[5]The MSE curves, and the flow profiles with the value of k_s obtained are shown in Appendix A.

Taking into account that the minimum water depth to be used in the streets of MURI will be approximately 3.5 cm (in order to obtain more complete information on the flow and be able to use the ADV as a measuring instrument), we will start from the premise that the minimum acceptable acquisition duration should allow a deviation of no more than 0.5% of the convergence value at 400 s for the smallest water depth value to be observed in the model, i.e. 0.5% of the minimum established value of 3.5 cm is 0.175 mm $\approx$ 0.2 mm.

Observing the figure 3.10 almost all the tests are within this criterion from the beginning, except two cases for the flow rate of 3 [l/s], in one of them this condition is obtained from 50 s, thus strictly speaking, 50 s should be the adequate duration of data acquisition.

It is important to mention that these measurements were performed under uniform flow conditions, so an extra check should be considered if there are different conditions where it can be observed that the flow surface is not completely stable.

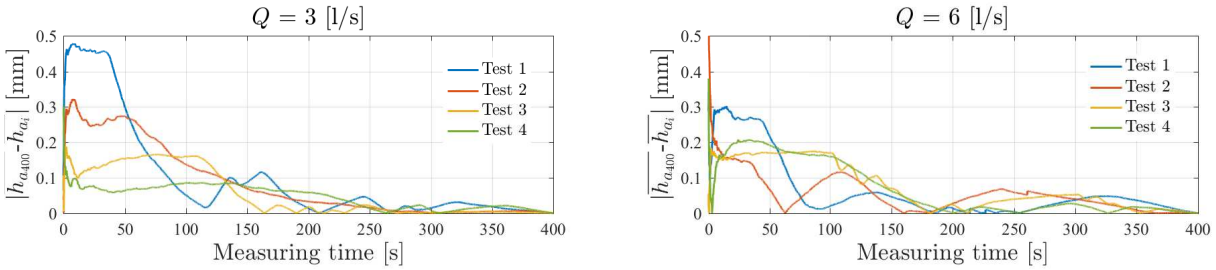

FIGURE 3.10. Difference between the time-averaged value in the total time and the time-averaged value for each instant.

In Appendix A, the graphs of the evolution of the flow rate during the measurements and the instantaneous values for each test are shown.

3.4.2 Water flow velocities

The flow velocities have been measured using an Acoustic Doppler Velocimeter, ADV (Vectrino+, Nortek, which measure the velocity in three dimensions. The velocimeter sends out a beam of acoustic waves at a fixed frequency from a transmitter probe, these waves bounce off of moving particulate matter in the flow and the probe detect for the change in frequency of the returned waves. For this reason the flow requires artificial introduction of particles (seeding the flow).

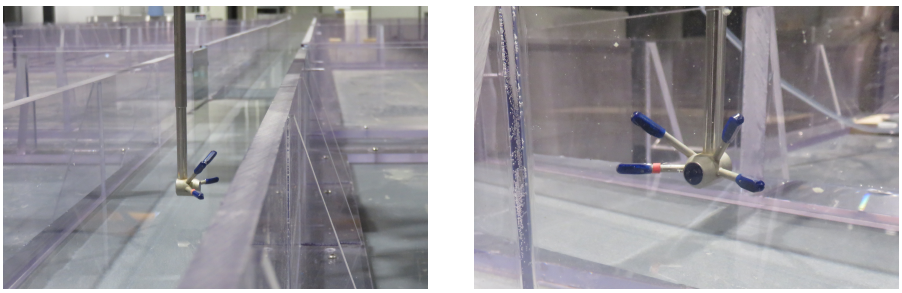

FIGURE 3.11. Acoustic Doppler Velocimeter.

The convergence of the signal was tested in order to know the appropriate acquisition duration for the measurements to obtain flow parameters and turbulence statistics. These tests were performed by measuring for 600 seconds at a rate of 100 Hz, and they were carried out in three different locations; close to the surface, close to the bottom and close to the wall.

According to the manufacturer, the device has an accuracy of 0.5% of the measured value, therefore this criterion has been taken into account to determine the appropriate acquisition duration for the measurements.

In each independent test the mean flow velocities in the three directions (x, y, z) were obtained as a function of the measured time to observe the moment when these flow velocities remained more or less constant. The following figure shows the results for one of these tests, the results of the other two tests are shown in Appendix A.

Observing the convergence results for the flow velocity and for the turbulence parameters, 50 seconds acquisition duration is sufficient to be within the deviation range of 0.05% of the final convergence value (in this case the value obtained with an acquisition time of 600 s), see figure 3.13. However, for parameters such as transverse flow velocities, and fluctuations, it is not possible to use this criterion, and it has been found that to obtain reliable data from these parameters it is necessary to take an acquisition duration no less than 200 seconds.

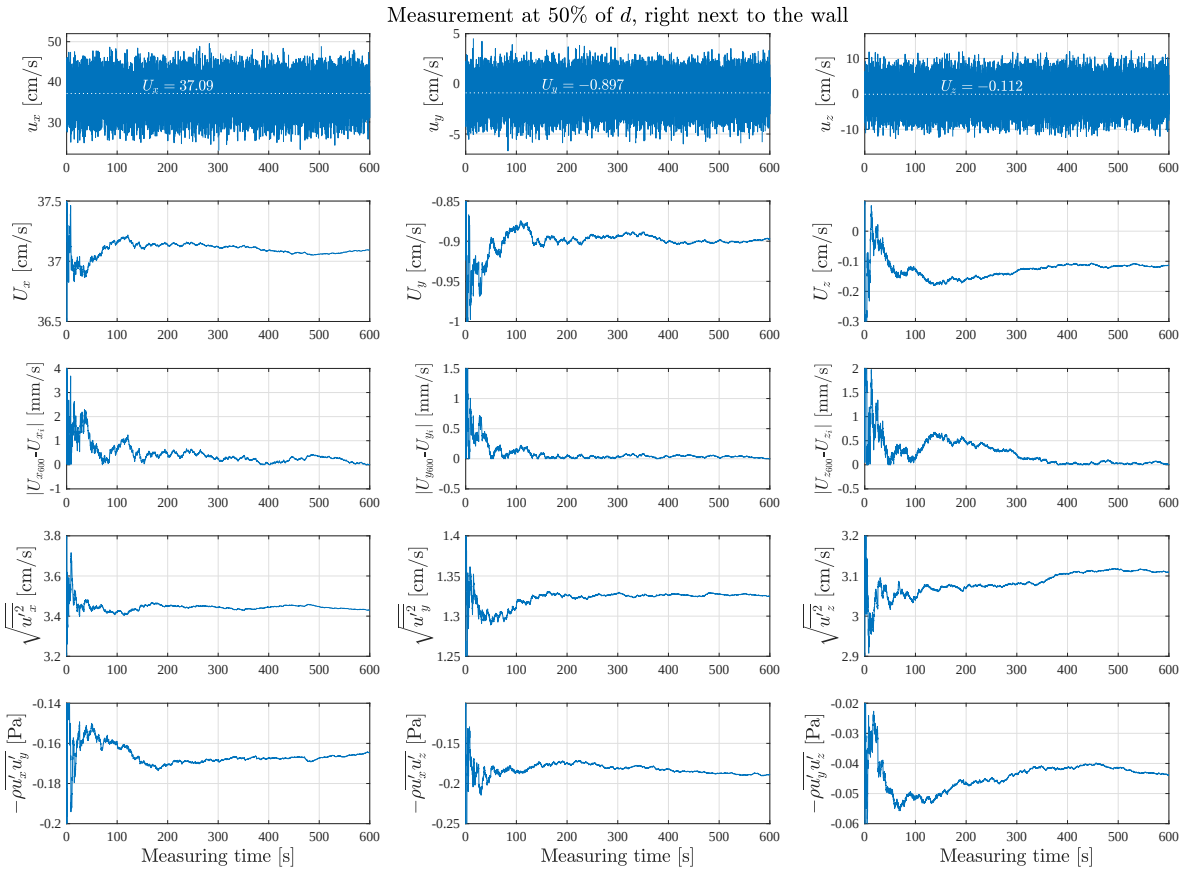

FIGURE 3.12. From top to bottom, the first line of graphs shows instantaneous flow velocity, second line the time-averaged velocity, the third line shows the difference between the total and for each instant averaged velocities, the two remaining lines show turbulence parameters, the standard deviation of the set of velocity fluctuations and the Reynolds-stress respectively.

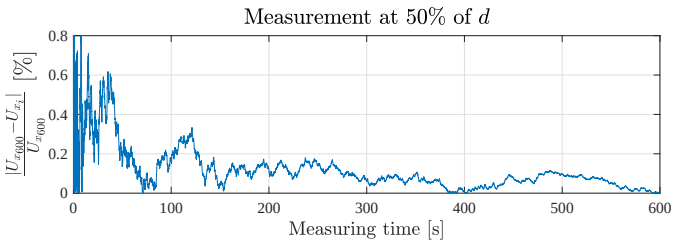

FIGURE 3.13. Percentage of deviation between the final convergence value and the value at each instant.

3.5 Configurations in MURI to be studied

3.5.1 Simple street

In MURI a uniform flow will be established in the right street, which is isolated from the other streets and has a constant rectangular cross section along its entire length, which makes it a straight prismatic section channel. (see figure 3.14). A slope of the floor smaller than the critical slope will be used to maintain the flow in subcritical regime.

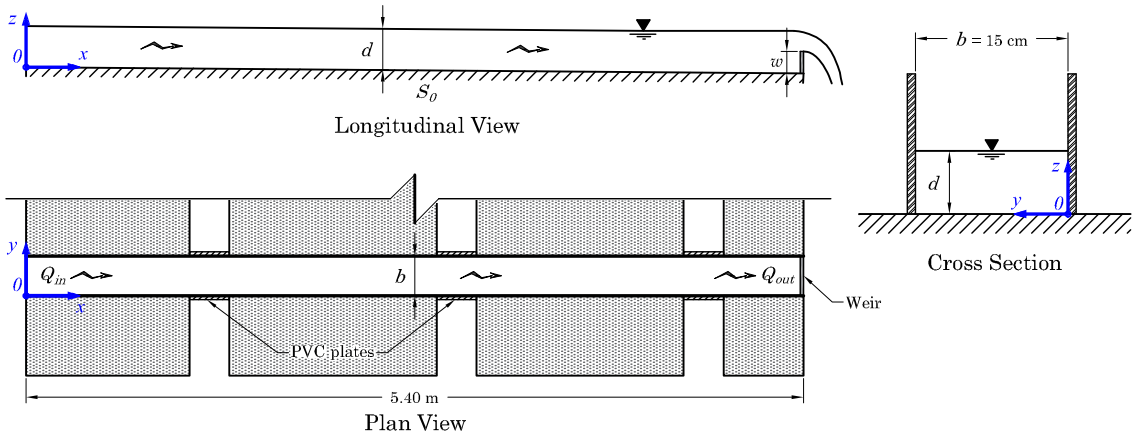

FIGURE 3.14. Scheme of the right longitudinal street in MURI.

Due to the variation of slope in the model and as the length of the street is not long enough to establish uniform flow, a weir will be used in the outlet area (downstream control) to increase the water depth and quickly reach the normal depth line.

3.5.2 Street with cavities

The PVC plates blocking the central transverse street will be moved to obtain a cavity configuration as shown in the figure 3.15

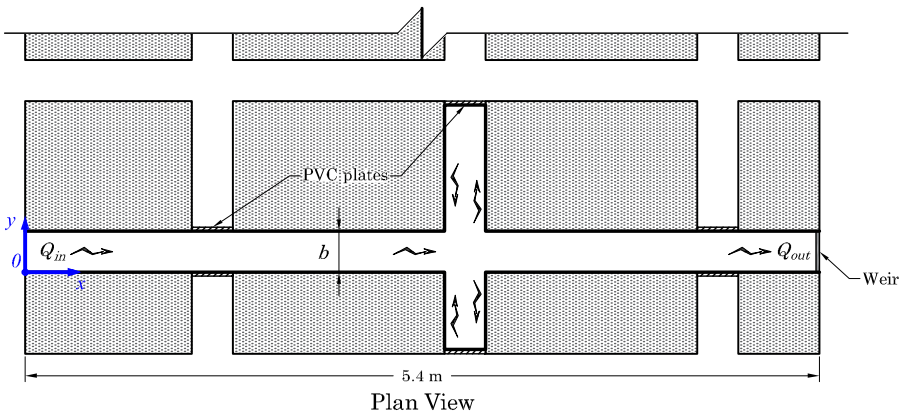

FIGURE 3.15. Scheme of the right longitudinal street in MURI under cavity configuration.

The flow rate, slope and height of the downstream weir will be the same to the above configuration. With this it will be possible to observe the influence of cavities, compare the results with those obtained previously, and know how the model and the measuring instruments behave under this configuration.

Chapter 4

Results

4.1 Simple street (straight flume)

4.1.1 Establishing uniform flow

A flow rate of 3 l/s, and a slope in the model of 0.1 % (plus the existing slopes in the floor of the model, obtained in the previous chapter), were set in the model. After several tests modifying the height of the downstream weir, it was found that a value of 2 cm allowed to establish a quasi-uniform flow along the channel (street).

This flow begins to be noticed from the 1.7 m x-station, where the variation in water depth begins to be much smaller. The depth variation between this station and the last measuring station ($x = 5.2$ m) is 0.5 mm, see figure 4.1.

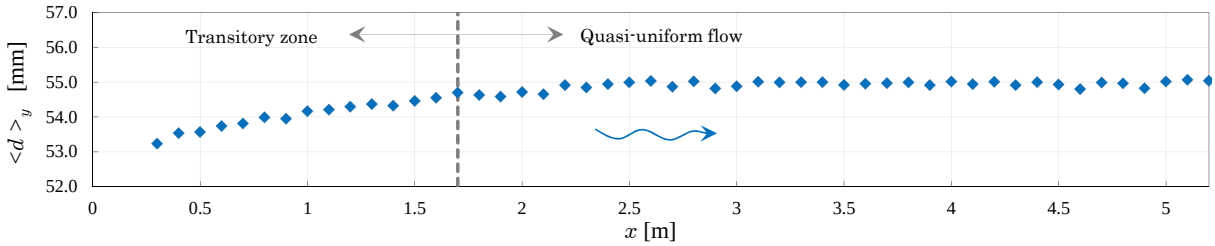

FIGURE 4.1. Water depth profile along the street, $Q = 3$ l/s.

The slope of the floor in this reach is 0.12 %, while the slope of the water surface is 0.11%, which confirms the quasi-uniform flow assumption. The following table shows the final values chosen which showed a very good approximation to the uniform flow, and the hydraulic parameters.

TABLE 4.1. Flow parameters.

Q [l/s]	S_0	w [cm]	b [cm]	$< d >_{xy}$ [cm]	b/d	U_b [cm/s]	k_s [cm$\times 10^{-3}$]	u_* [cm/s]	$\mathbf{R}$ [$\times 10^4$]	$\mathbf{F}$	$\mathbf{R}_*$
3.00	0.00120	2.00	15.00	5.49	2.73	36.43	3.60	1.93	4.62	0.50	0.70

From the values in the table above it can be concluded, that the channel is classified as a *narrow channel* ($b/d < 5$) according to Chow [4], and it is a *hydraulically smooth turbulent flow* ($\mathbf{R} > 12500$, and $\mathbf{R}_* \leq 5$).

With this flow established and after performing several tests to obtain the flow velocity and turbulence parameters, it has been found that the maximum velocity is approximately 70 % of the water depth (dip phenomenon). It was also found that the flow is not symmetrical in the channel, however, towards the end part (near the outlet) there is symmetry, see figure 4.4.

4.1.2 Correction of the asymmetric flow

The distribution of the flow velocity along the channel shows that the higher velocities have a clear inclination towards the left bank, however at the end of the reach, in station $x = 4.5$, a symmetric distribution can be observed, i.e. the flow becomes symmetrical as it moves away from the inlet.

Taking this into account, we can see that the problem is found when water goes from the tank to the channel, and even from the pipe that supplies the tank. Various changes in the direction of the pipe before entering the tank can cause the presence of eddies that reach the tank and provoke an unstable flow towards the street.

(a) (b)

FIGURE 4.2. Tank at the inlet of the street, (a) Initial configuration, with protection grille, (b) Configuration with the plastic grid over the grille.

There is a plastic grid, honeycomb type at the inlet of the channel, and at the entrance to the tank, after the pipe, there is a horizontal protection grille (see figure 4.2.a), which is also useful to dissipate the eddies coming from the pipe, however it is not enough, and it will be necessary to place some extra grid. Therefore, some grids and extra materials were placed in the tank and in the channel, with the intention of achieving a symmetrical flow.

As a first attempt it was placed a plastic grid over the existing grille in the tank (see figure 4.2.b) like the one on the channel, it has a thickness of 5 cm and is formed by circular cells of 0.8 cm in diameter. Together with this plastic grid, several layers of plastic filtering material (Japanese pond mat) have been placed, in order to keep the plastic grid in place, as well as to help dissipate any eddy coming from the pipe.

With this arrangement, the horizontal flow velocity distributions were obtained in different x-stations along the channel observing an improvement, however, not enough. Thus, the same process was continued until acceptable results were obtained that showed a more symmetric flow distribution (the different arrangements are shown in Appendix B).

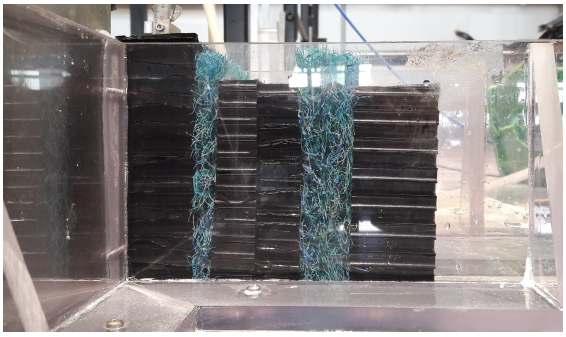

FIGURE 4.3. Final arrangement on the street, 2 plastic grids 5 cm thick, 2 plastic grids 2.5 cm thick and plastic filtering material.

The final arrangement consisted of the plastic grid and filter material placed horizontally in the tank, plus 4 misaligned plastic grids and filter material at the inlet of the channel (see figure 4.3).

With this, an improvement in the symmetry of the velocity distribution was observed (see figure 4.4), however, the flow capacity of the model was decreased. Due to the presence of plastic grids at the inlet, the energy losses between the channel and the tank increased, and the charge on the tank increased as well, making impossible to establish a flow rate greater than 3.5 l/s without overflow.

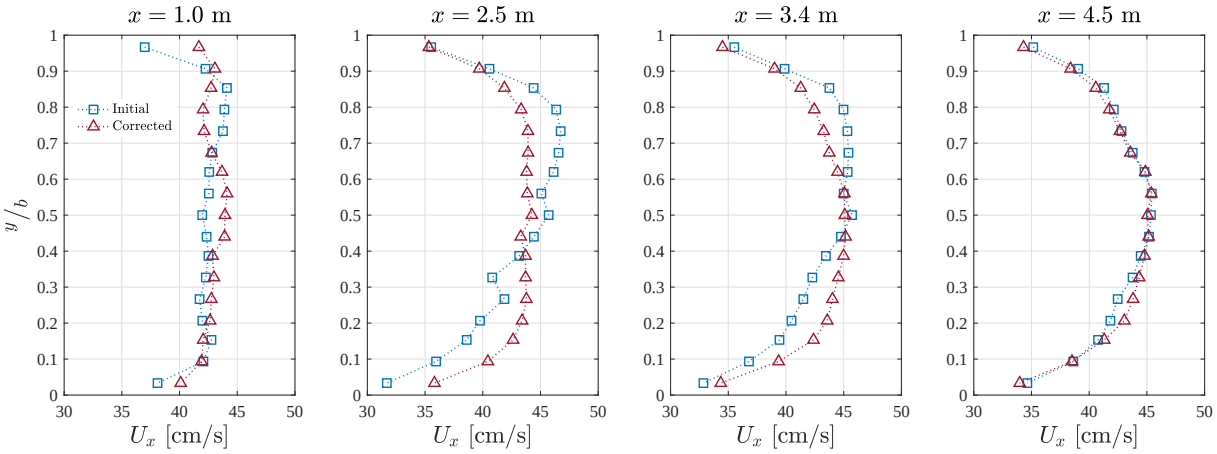

FIGURE 4.4. Transverse distributions of time-averaged streamwise velocity, U_x, at 70% of d and at various downstream x-stations. In blue, the initial configuration where the asymmetric flow was observed, in red, the final arrangement where an improvement in the flow symmetry was observed.

With the corrected flow, the profiles of the water depth and the flow surface were again obtained, and with these the different hydraulic parameters. Some parameters and the slope of the water surface remained the same ($S_w = 0.11\%$), the average water depth varies slightly by 0.2 mm. The following table shows the final values.

TABLE 4.2. Corrected flow parameters.

Q [l/s]	S_0	w [cm]	b [cm]	$< d >_{xy}$ [cm]	b/d	U_b [cm/s]	k_s [cm$\times 10^{-3}$]	u_* [cm/s]	**R** [$\times 10^4$]	**F**	$\mathbf{R}_*$
3.00	0.00120	2.00	15.00	5.51	2.72	36.30	3.60	1.93	4.61	0.49	0.70

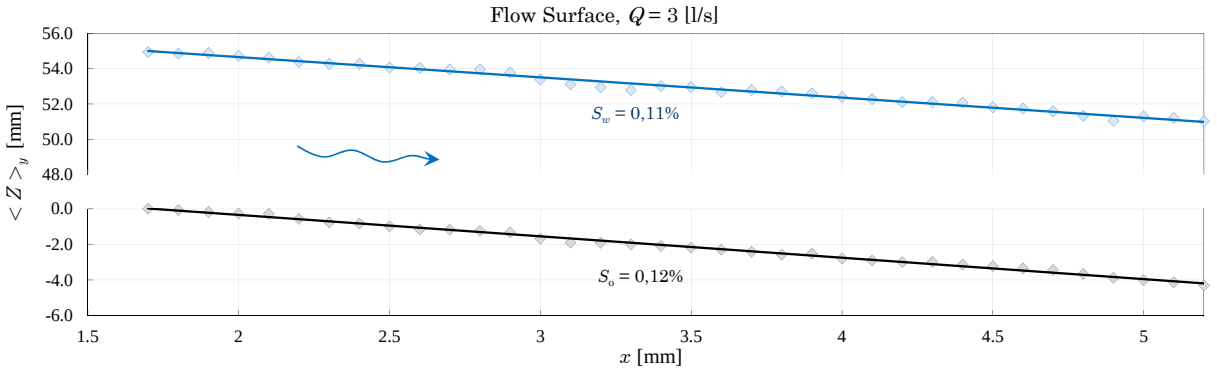

FIGURE 4.5. Flow surface profile and floor profile along the street.

4.1.3 Velocity distribution

Vertical velocity distributions were obtained at the centerline of the channel ($y/b = 0.5$) for different x-stations, in the reach where the uniform flow was established.

In figure 4.6 the time-averaged streamwise velocities are shown, the red line represents the theoretical logarithmic law of velocity distribution. The results show that the velocities follow the log-law, however, when approaching the free surface a deviation is clearly observed (dip phenomenon). The maximum flow velocity is between 70 and 80 % of the water depth, which is consistent with results obtained by several researchers. In general, they have reported that the distance from the free surface where the maximum velocity is observed is greater when the aspect ratio, b/d is lower. For instance, Sarkar [13] found the maximum velocity at 60 % of d, and Nezu *et al.* [11] at 65 %, both for an aspect ratio of 2.

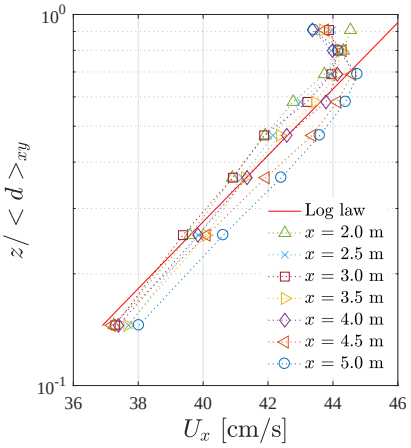

FIGURE 4.6. Vertical distributions of time-averaged streamwise velocity, U_x, at various downstream x-stations.

The vertical distributions of Reynolds shear stress are shown in figure 4.7, in open channel flow this stress follows the traditional linear law [13], which is what we see in the figure. Due to the measuring instrument, the water depth and the model size, it was only possible to obtain data up to 60% of the flow depth.

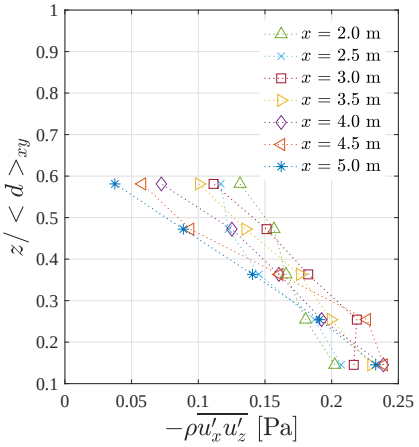

FIGURE 4.7. Vertical distributions of Reynolds shear stress in the xz-plane, at various downstream x-stations.

In Appendix B, the flow velocity, flow velocity fluctuations and Reynolds stress distributions are shown for the different flow directions.

Cross-sectional distribution of velocity was obtained for different x-stations, the velocities were nondimensionalised by the bulk velocity, U_b, in order to be able to compare them. For each section its possible to observe the symmetry of the flow, as well as the evolution of the dip phenomenon along the y-axis, which according to Auel *et al.* [1], it is more noticeable in the corner regions and decreases toward the centerline.

The flow correction performed, in addition to improving the symmetry in the channel, showed a slight improvement in turbulence by decreasing the flow velocity fluctuations (In Appendix B, figures of flow velocity distributions and fluctuations before and after flow correction are shown).

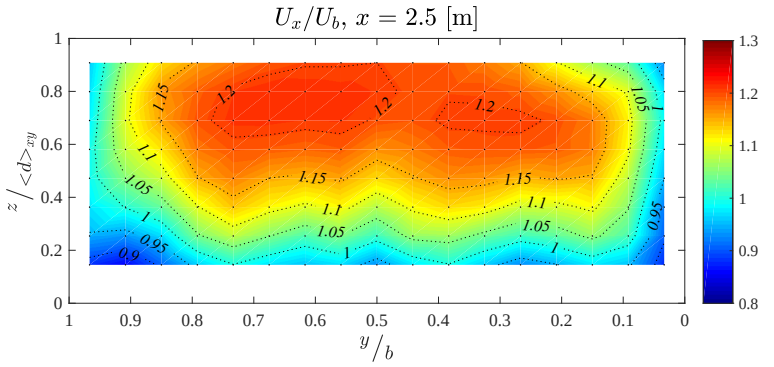

FIGURE 4.8. Cross-sectional distribution of dimensionless time-averaged streamwise velocity, U_x.

The spanwise and vertical velocities have had to be corrected[1], with the purpose of

[1]The measurements to obtain the velocities throughout the cross section were made in two stages due to the dimensions of the ADV and the channel; in the first stage a half cross section was measured, and for the second stage, the ADV was rotated 180 degrees and the remaining half cross section was measured , for this reason the correction was made independently for each half section, because the whole section cannot be corrected with the data of a single half section.

getting more reliable data according to different applicable criteria for a uniform flow . In the case of spanwise velocities (y-direction), the following criteria are considered:

- Criterion 1. The average velocity right next to the wall is zero, $\int_0^d U_y \, \mathrm{d}z = 0$ at $y/b \approx 1$.
- Criterion 2. The average velocity in the half cross section is zero, $\int_0^{0.5b} \int_0^d U_y \, \mathrm{d}z\mathrm{d}y = 0$.

For vertical velocities, the following criterion are considered:

- Criterion 1. The average velocity right next to the bottom is zero, $\int_0^{0.5b} U_z \, \mathrm{d}y = 0$ at $z \approx 0$.
- Criterion 2. The average velocity in the half cross section is zero, $\int_0^{0.5b} \int_0^d U_z \, \mathrm{d}z\mathrm{d}y = 0$.

The z-axis and y-axis rotational matrices were used to correct the spanwise and vertical velocities respectively. The rotation angles were obtained in three different x-stations, the values obtained are presented in the table C.1.

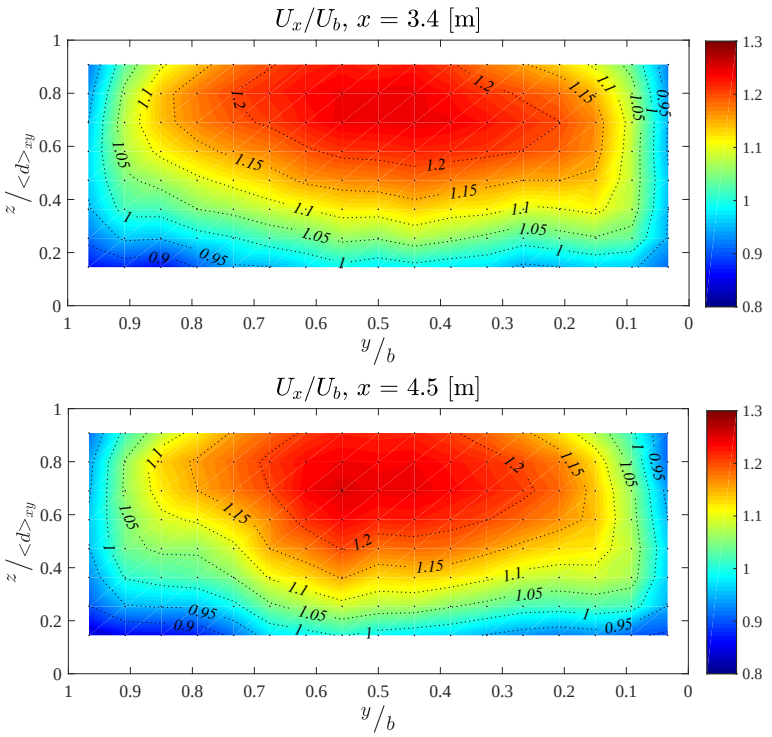

FIGURE 4.9. Cross-sectional distribution of dimensionless time-averaged streamwise velocity, U_x, for different x-stations.

The rotation angles obtained for each station and with each criterion are similar, much more similar in the case of criterion 1 for the correction of spanwise velocities (θ_z), which shows that the channel walls are well aligned and straight.

TABLE 4.3. Correction angles according to the different criteria established.

Half section		**Left**			**Right**		
x-station [m]		**2.5**	**3.4**	**4.5**	**2.5**	**3.4**	**4.5**
θ_z [°]	Criterion 1	1.42	1.35	1.43	3.17	3.27	3.16
	Criterion 2	1.02	0.99	0.93	3.63	3.68	3.64
θ_y [°]	Criterion 1	0.12	-0.01	-0.12	-0.07	0.02	-0.01
	Criterion 2	-0.34	-0.47	-0.59	-0.87	-0.80	-0.83

The correction of the transverse velocities was finally carried out with criterion 1 for both cases, in the case of vertical velocities, the area without data in the half cross section is more than 50%, so criterion 2 was discarded. For spanwise velocities, both criteria were compared using as reference the results presented by Nezu *et al.* [11] for secondary currents in narrow channels, the values that best adjusted were those obtained with criterion 1.

With the transversal velocities corrected, the cross-sectional velocity distribution was obtained for the same x-stations, they were nondimensionalised by the bulk velocity, U_b, which is very similar to the average streamwise velocity[2], $< U_x >_{yz}$. Then we can compare the magnitude

[2]Time-averaged streamwise velocity averaged spatially in the cross section, the value is around $0.98U_b$

of the secondary currents with respect to the streamwise velocity, and note that the maximum spanwise velocity is between 3 and 4 % of the streamwise velocity, in the case of the maximum vertical velocity, it is between 1 and 1.5 %.

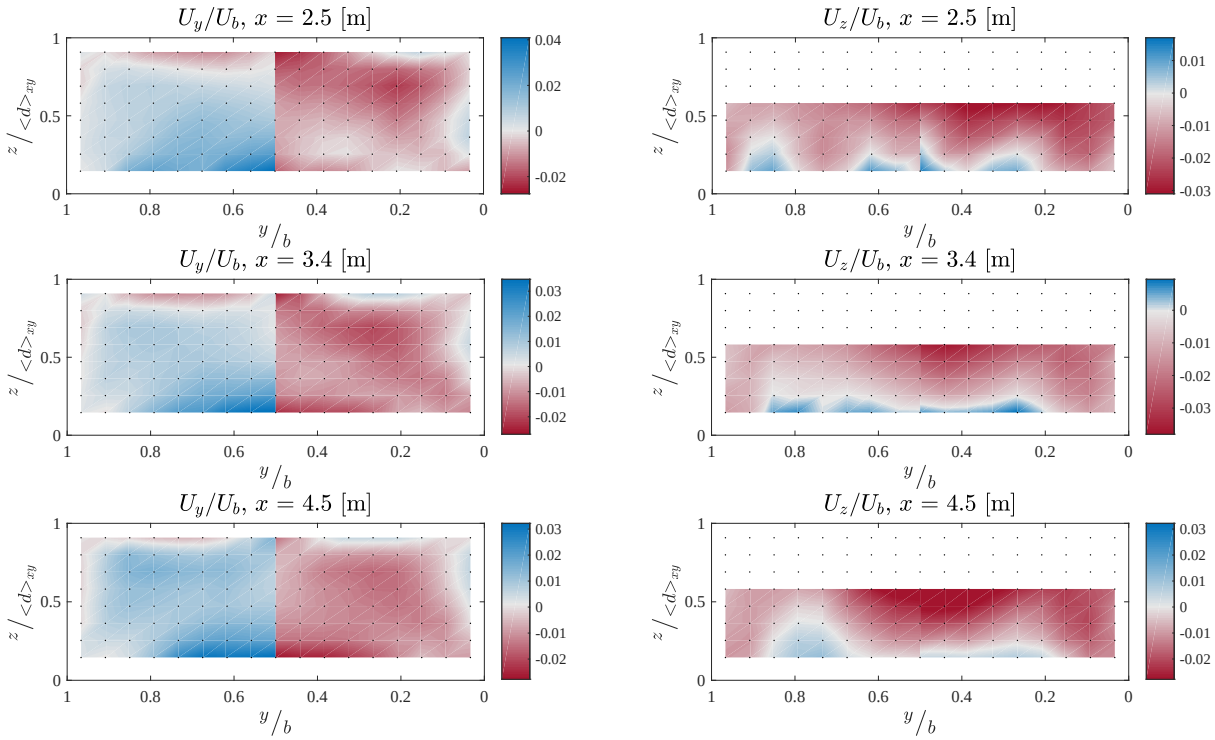

FIGURE 4.10. Cross-sectional distribution of dimensionless time-averaged spanwise and vertical velocities, U_y and U_z.

The velocity vectors U_yU_z were plotted in the different cross-sections, they were also nondimensionalised by U_b, and it has been found that the maximum velocity of the secondary flow is between 3 and 4 % of the mainstream velocity. The vectors direction is similar to the one presented by Nezu *et al.* [11], however it is not possible to see clearly the vortices (see figure 4.11), in the upper part mainly because of the lack of data on vertical velocities, however in this area the spanwise velocity vectors (red vectors) are shown, and because of the change of direction appreciated, it is possible to think that there is a vortex in that area. The complete cross section of secondary current vectors for the different x-stations are shown in Appendix B.

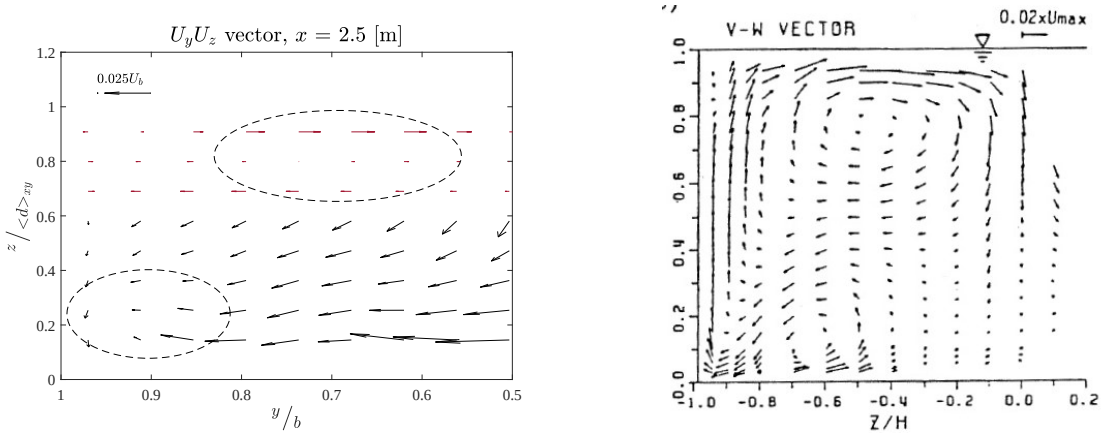

(a) (b) Nezu *et al.*, 1993

FIGURE 4.11. Half cross section of secondry current vectors. In figure (a), the areas surrounded by the dashed line are where vortices may occur due to the change in direction observed in the vectors.

4.2 Street with lateral cavities

4.2.1 Flow characteristics

With this configuration, water depths were obtained at various stations along the channel (street). Apparently, the presence of the lateral cavities has caused an increase in the flow depth in the upstream reach, approximately 1 mm on average, with respect to the water depth in the previous configuration. From the stations where the cavities are located, the water depth begins to decrease rapidly and 0.1 m after them, increases again until it is more or less stable and uniform, with a water depth value similar to the previous configuration, see figure 4.12.

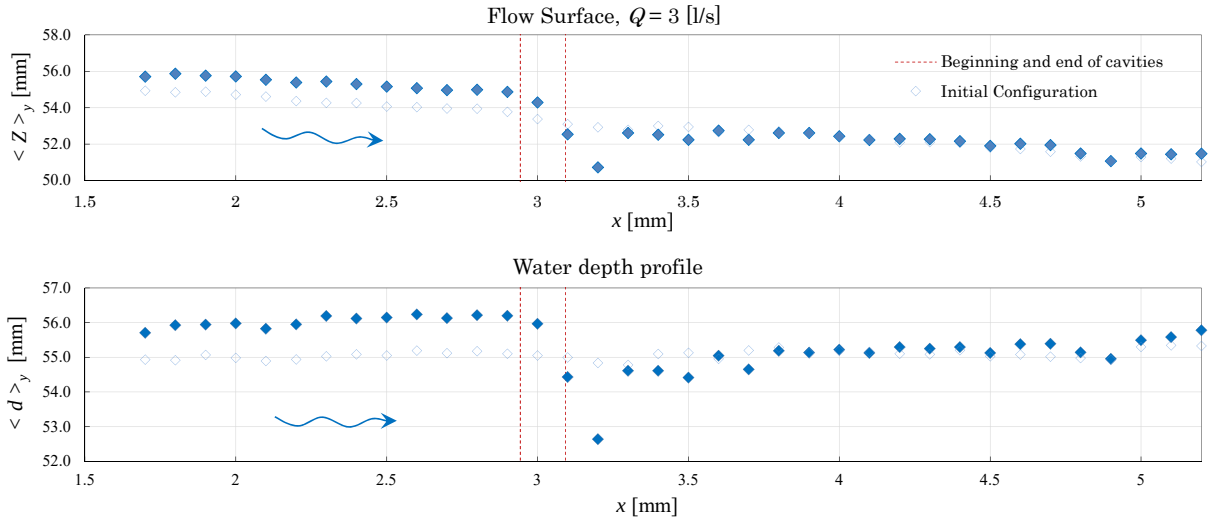

FIGURE 4.12. Comparison of water depth and flow surface between the simple street configuration (initial configuration) and the street with the cavities.

With these conditions the different hydraulic parameters were obtained in the same reach analysed in the simple street configuration. On average, water depth increased 0.3 mm, thus the average flow velocity decreased very slightly, and the other parameters remained almost the same. The following table shows the values.

TABLE 4.4. Flow parameters for the street with lateral cavities.

Q [l/s]	S_0	w [cm]	b [cm]	$< d >_{xy}$ [cm]	b/d	U_b [cm/s]	k_s [cm$\times 10^{-3}$]	u_* [cm/s]	**R** [$\times 10^4$]	**F**	$\mathbf{R}_*$
3.00	0.00120	2.00	15.00	5.54	2.71	36.10	3.60	1.94	4.60	0.49	0.70

4.2.2 Velocity distribution

As in the previous configuration, vertical distributions of flow velocity and turbulence parameters were obtained. The dip phenomenon is most clearly observed in downstream stations, and the velocity fluctuations increased, most notably in the spanwise velocity in reference to the previous configuration (see figure 4.13.b).

Also the maximum flow velocity increased in the downstream zone after the cavities, although the water depth remained more or less similar in this reach, the velocity distribution had a slight shift, mainly in the 3.5 and 4 m x-stations, where the velocity difference between the zone near the surface and the zone at 70% of the flow depth (zone where the maximum velocity is) is more noticeable, see figure 4.13.a.

The appendix C, shows the distribution of flow velocities and turbulence parameters at different stations along the channel and for the 3 different flow directions.

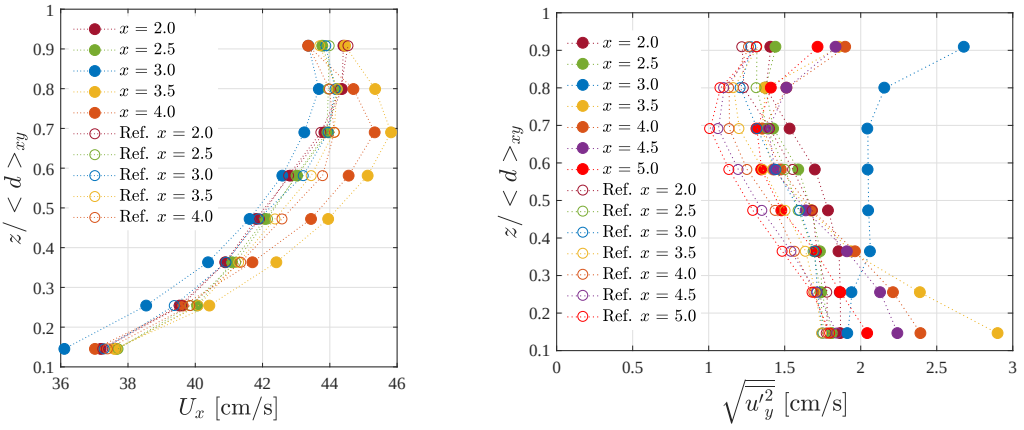

(a) (b)

FIGURE 4.13. a) Vertical distribution of time-averaged streamwise velocity for the x-stations close to the cavities. b) Vertical distribution of spanwise velocity fluctuations. Reference (Ref.) refers to simple street configuration.

In this configuration of lateral cavities, also were obtained the cross-sectional distribution of flow velocity in the same x-stations, the spanwise and vertical velocities were corrected with the same criteria explained in the previous subchapter (the correction angles are shown in table C.1 of Appendix C).

The velocities were nondimensionalised by U_b, the figures 4.14 and 4.15 show the distributions of the streamwise velocity, a more symmetrical flow is clearly observed than in the previous configuration, however, although the maximum velocity is in the central area of the cross section, there is a slight shift to the left bank, noticeable with the help of the isovels, possibly due to the presence of the cavities, which have a different length, this effect is visible in the downstream reach.

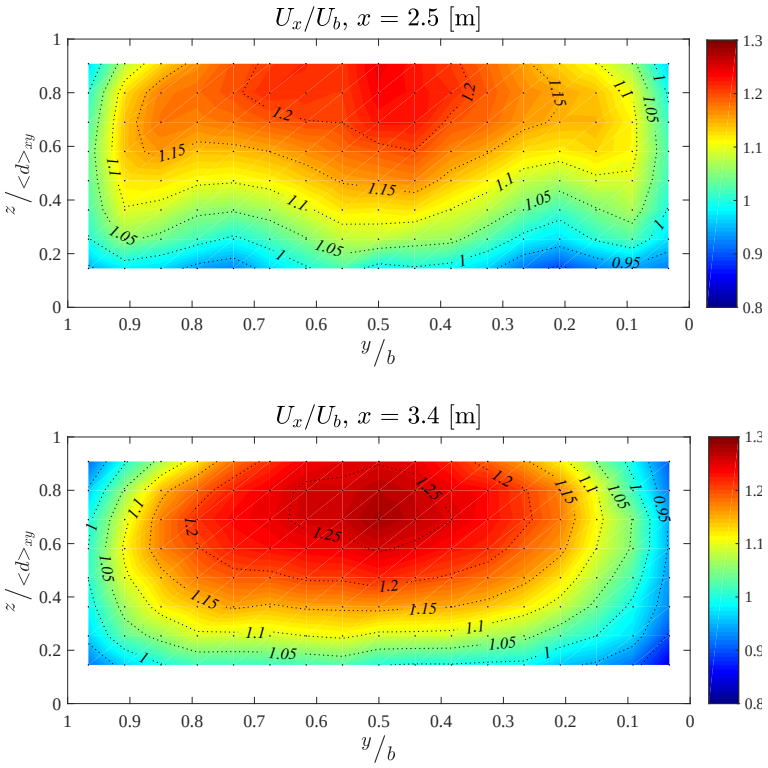

FIGURE 4.14. Cross-sectional distribution of dimensionless time-averaged streamwise velocity, U_x, for different x-stations.

With the corrected transverse flow velocities, the velocity vectors U_yU_z were plotted in the different cross-sections, to observe the behavior of the secondary currents. In this case, unlike the vectors of the secondary currents of the previous configuration, it has been possible to observe the vortex in the bottom corner of the cross section for the 2.5 m x-station.

In the figure 4.16, the area surrounded by the blue dashed line shows the vortex in a position similar to that shown by Nezu [11] in figure 4.11.b.

For the 3.4 m x-station it is also possible to see the vortex of the bottom on the right bank. The vortex near the surface has again not been clearly distinguished due to the lack of data in the upper zone, but the change in direction of the spanwise velocities in that zone suggests that the vortex is there. The complete cross section of secondary current vectors for the different x-stations are shown in Appendix C.

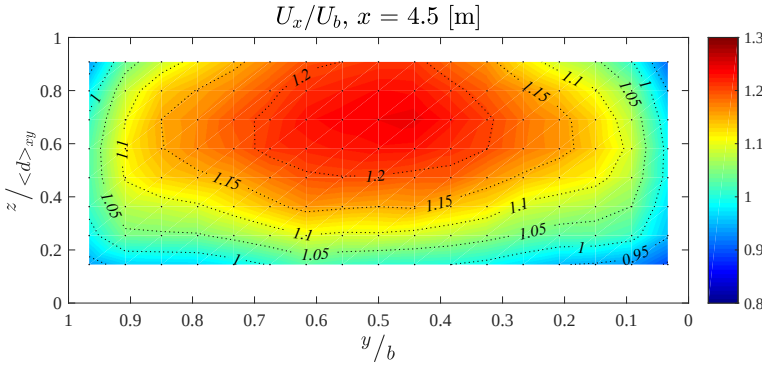

FIGURE 4.15. Cross-sectional distribution of dimensionless time-averaged streamwise velocity, U_x.

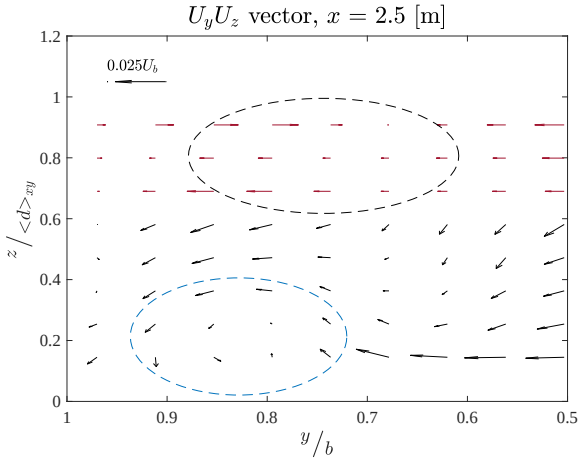

FIGURE 4.16. Half cross section of secondary current vectors.

4.2.3 Cavities

Cavity flows are characterized by complex flowfeatures such as quasi-periodic vortices produced at the interface between the main flow and the cavity, multiple recirculating zones, and coherent vortical structures in the cavity that interact with each other and with the walls, Mignot *et al.*[10].

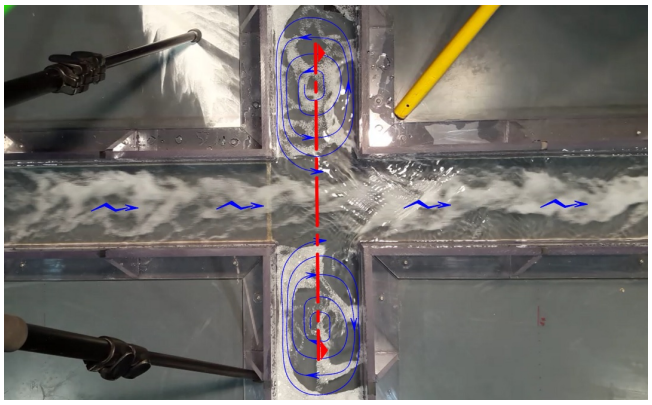

FIGURE 4.17. Top-view of cavities in MURI, the dashed red line represents the centerline of the cavities.

Measurements were made with the ADV along the centerline of the cavities, from the left cavity to the right cavity as shown in figure 4.17 (dashed red line). The results obtained are shown in the figure 4.18, it is possible to observe the difference of the streamwise velocity between the main channel and the cavities, this velocity gradient formed at the cavity-channel interface is known as the mixing layer.

Although the maximum velocity is near the central zone of the channel, the displacement of the flow towards the left bank is again very clearly observed. The mixing layer of the left side is inside the cavity, we observe the maximum gradient in this zone, while the mixing layer of the right side is located in the main channel.

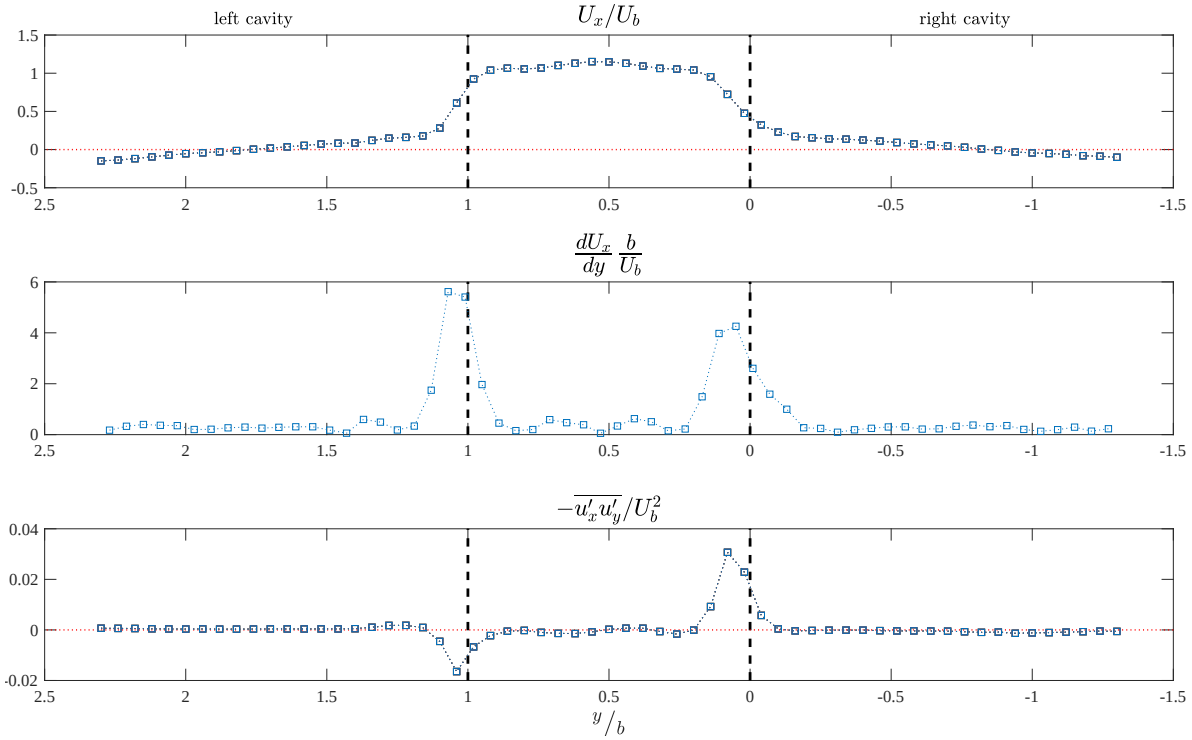

FIGURE 4.18. Spanwise distribution of dimensionless time-averaged streamwise velocity U_x, dimensionless spanwise gradient of time-averaged streamwise velocity $\frac{\mathrm{d}U_x}{\mathrm{d}y}$, and dimensionless Reynolds shear stress in the streamwise direction $-\overline{u'_x u'_y}$ in the centerline of the cavities. The black dashed lines represent the interface between cavities and main channel.

The results obtained have been compared with those obtained by Mignot *et al.* [10] (see figure 4.19), who studied a cavity on the right bank, which is the same width as the main channel, as in this case.

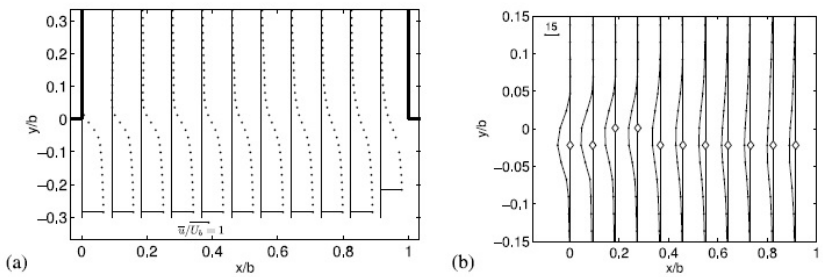

FIGURE 4.19. a) Spanwise distribution of dimensionless time-averaged streamwise velocity, and b) dimensionless spanwise gradient of time-averaged streamwise velocity (white symbols indicate the location of maximum gradient), along the mixing layer. The flow goes left to right; $y/b = 0$ represents the interface between the cavity and the main channel, and distributions for different positions are displayed along the interface [Mignot *et al.*, 2016].

4.3 Flow rate

As part of the tests to be performed on the model, the flow rates were obtained from the velocity measurements made on the cross sections, the intention is to know how reliable these measurements can be to obtain the flow rate in different zones and under different conditions.

Due to the physical characteristics of the ADV, there is a zone without data in the whole contour of the cross section, the zones near the walls (0.5 cm), the zone near the floor (0.7 cm) and the zone near the flow surface (0.5 cm).

In order to calculate the flow rate from the whole cross section, two methods have been proposed, which will be compared to know which one provides a better approximation to the flow rate recorded in the flowmeter.

- Method 1. Take a zero flow velocity on walls, floor and free surface, and compute a linear interpolation between these surfaces and the velocity values recorded on the external contour area.
- Method 2. Take on the walls, the floor and the free surface the same velocities recorded in the external contour area.

The results are shown in the following table, and *method 1* generates better results, in all cases a value lower than the expected flow rate, therefore, it may be possible to propose an adjustment factor that multiplies the calculated value to get closer to the expected value. For instance, with this amount of data, the factor that best fits is 1.02.

Adjusting the values with this factor produces a much lower percentage of error than that obtained without correction, however, it will require a larger population of data to find a more reliable adjustment factor, in addition to checking for different flow rate values.

TABLE 4.5. Flow rates calculated from velocity profiles, in [l/s].

x-station [m]	$\overline{Q}_{flowmeter}$	$Q_{Method1}$	$Q_{Method2}$
Simple street			
2.5	3.0	2.938	3.232
3.4	3.0	2.936	3.227
4.5	3.0	2.918	3.205
Street with cavities			
2.5	3.0	2.931	3.230
3.4	3.0	2.977	3.275
4.5	3.0	2.953	3.253

Chapter 5

Conclusions

It was found that the PVC plates that form the floor of the model are slightly misaligned, with a different slope each one, so this must be taken into account when performing the tests in order to generate more reliable measurements.

The tests carried out showed that the model is very sensitive to slight changes in the supply tank, generated by factors such as the number of pumps operating, as well as the operation of the other models found in the hydraulic room. For this reason, the most reliable way to set the flow rate in the model is using the *automatic mode*, although it fluctuates weakly, it remains constant on average over time. In manual mode, although the fluctuations are more uniform, it was observed that there are deviations of the average flow rate over time.

Convergence testing of the measuring instruments resulted in a long acquisition duration, 50 s for the ultrasonic distance sensor, and 200 s for the velocimeter (ADV). This can be explained by the fluctuations in the flow rate, which has a direct influence on the values recorded.

The flow homogeneity was corrected in the right longitudinal street, but this gives us indications that it should also be corrected in the other streets. The correction forced to put several grids in the street, which decreased the flow capacity, so it seems more convenient to put the grids in the tank upstream of the street, however it would be necessary to study if this will be sufficient and what options are available for flow rates greater than the 3 l/s used during these experiments.

The velocities and turbulence parameters in the streamwise direction seems to be quite reliable, the flow rate values obtained are very close to the expected values, so it can be said that this instrument (ADV) works very well for this purpose, however, for secondary currents, the dimensions of the model and instrument make impossible to take data near the floor and near the flow surface, resulting a very large blind area that does not allow to clearly identify the secondary currents. It would be good to try a complementary device, that allows to improve the readings in these points and thus to generate more complete information.

As forward-looking works, they are the reviewing the flow symmetry in the other streets, implementing the improvements to use larger flow rates in the model, such as 5 or 6 l/s, as well as obtaining the topography of the cross streets.

Appendices

Appendix A

Model characterization

A.1 Streets floor elevations

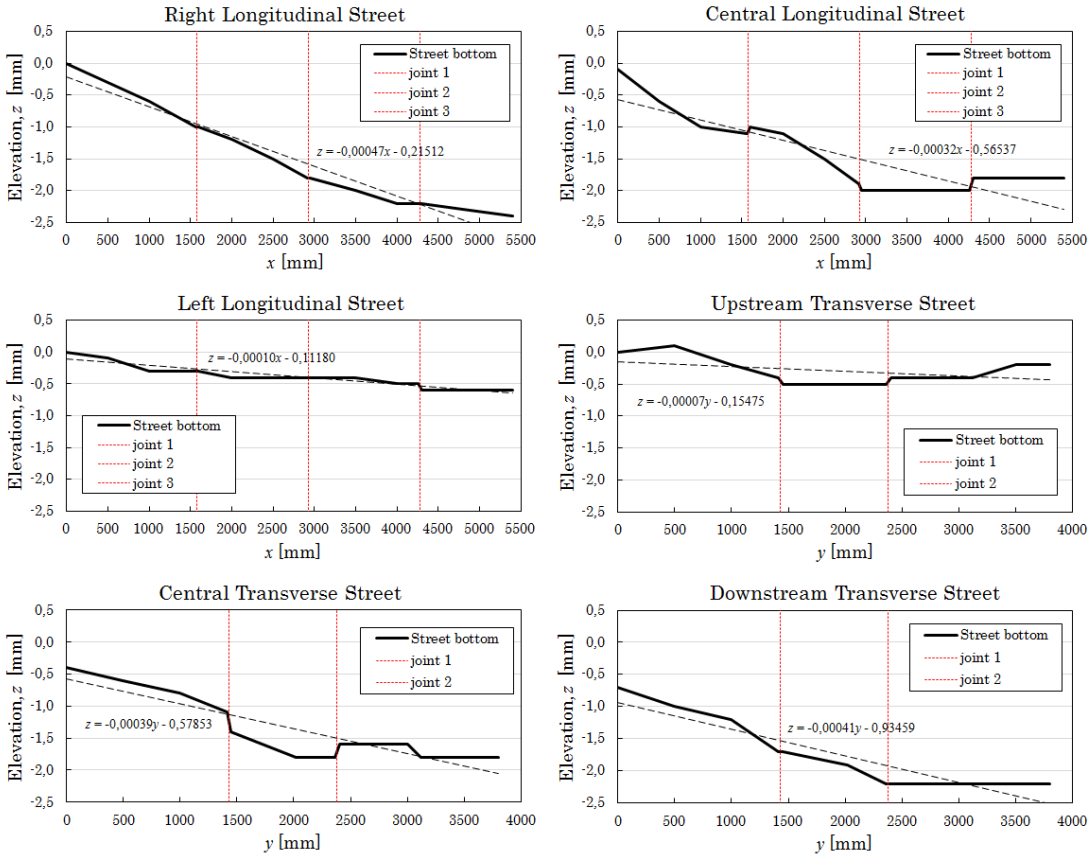

FIGURE A.1. Street floor elevations using a laser beam.

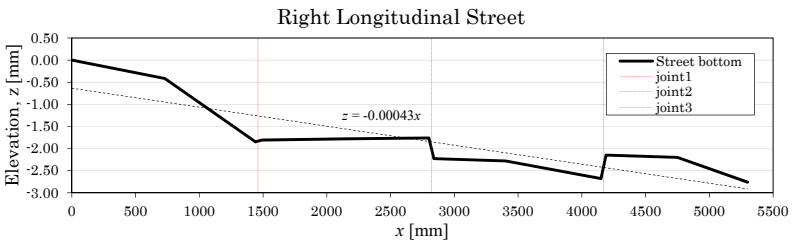

FIGURE A.2. Street floor elevations using a theodolite.

A.2 Flow rate fluctuation

TABLE A.1. Statistical parameters of the flow rate data series, values in [l/s].

Time	**Mode**	**Automatic**					**Manual**				
[min]	Q_s	2.00	3.00	4.00	5.00	6.00	2.00	3.00	4.00	5.00	6.00
100	μ	2.00	3.00	4.00	5.00	6.00	2.08	3.01	4.02	4.94	5.87
	σ	0.02	0.03	0.03	0.03	0.06	0.02	0.02	0.04	0.04	0.05
0 - 20	μ	2.00	3.00	4.00	5.00	6.00	2.06	3.03	4.01	4.98	5.96
	σ	0.03	0.03	0.02	0.04	0.05	0.01	0.01	0.02	0.02	0.02
20 - 40	μ	2.00	3.00	4.00	5.00	6.00	2.06	3.02	4.01	4.97	5.89
	σ	0.02	0.03	0.02	0.03	0.06	0.01	0.01	0.02	0.02	0.04
40 - 60	μ	2.00	3.00	4.00	5.00	6.00	2.08	3.00	4.01	4.96	5.84
	σ	0.02	0.02	0.03	0.02	0.07	0.01	0.01	0.02	0.02	0.02
60 - 80	μ	2.00	3.00	4.00	5.00	6.00	2.08	3.00	4.01	4.94	5.84
	σ	0.01	0.03	0.04	0.04	0.06	0.01	0.01	0.02	0.04	0.02
80 - 100	μ	2.00	3.00	4.00	5.00	6.00	2.10	3.02	4.07	4.88	5.84
	σ	0.03	0.02	0.04	0.04	0.07	0.01	0.02	0.04	0.02	0.02

A.3 k_s values for different discharge values

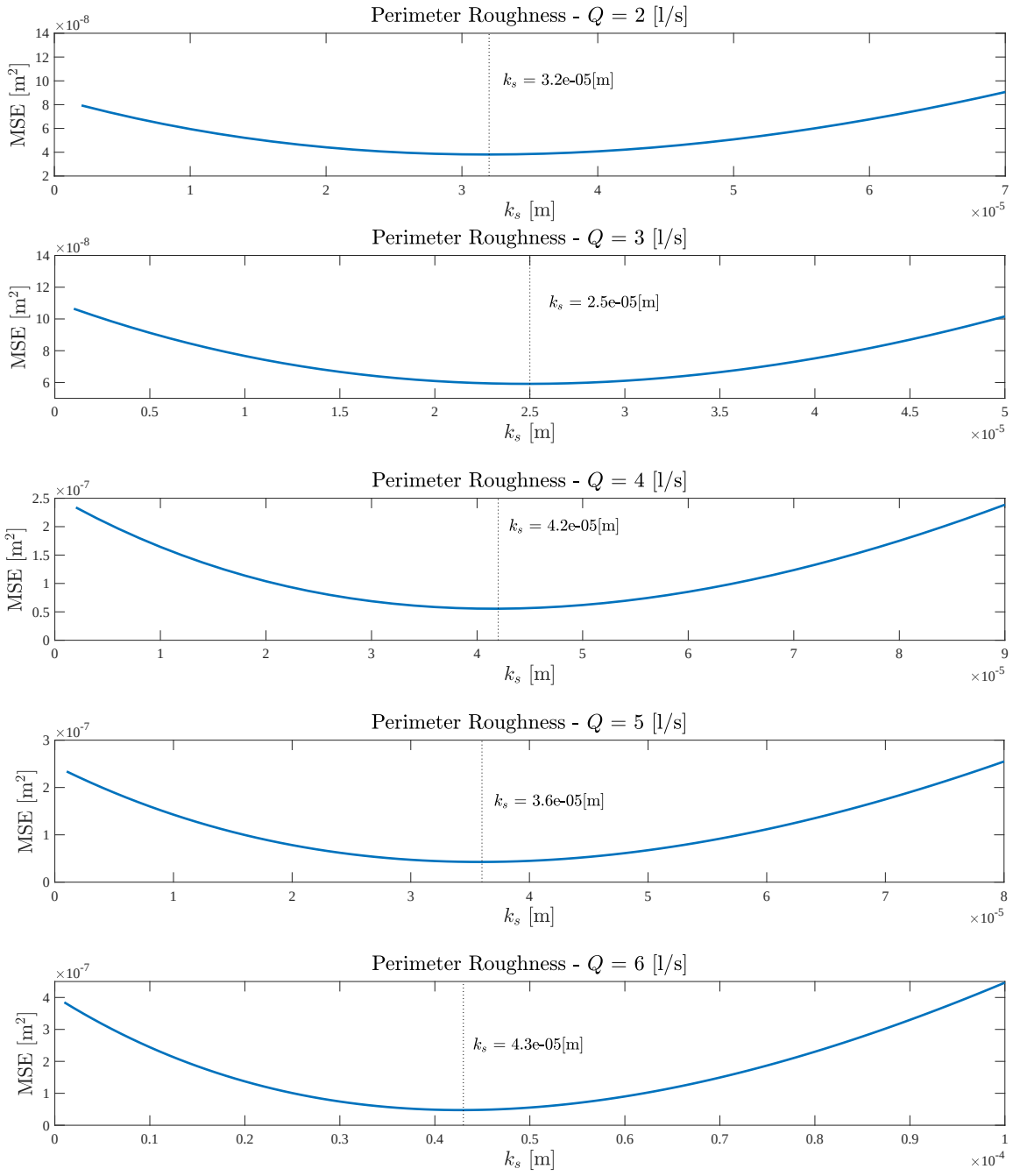

FIGURE A.3. Mean square error for different k_s values.

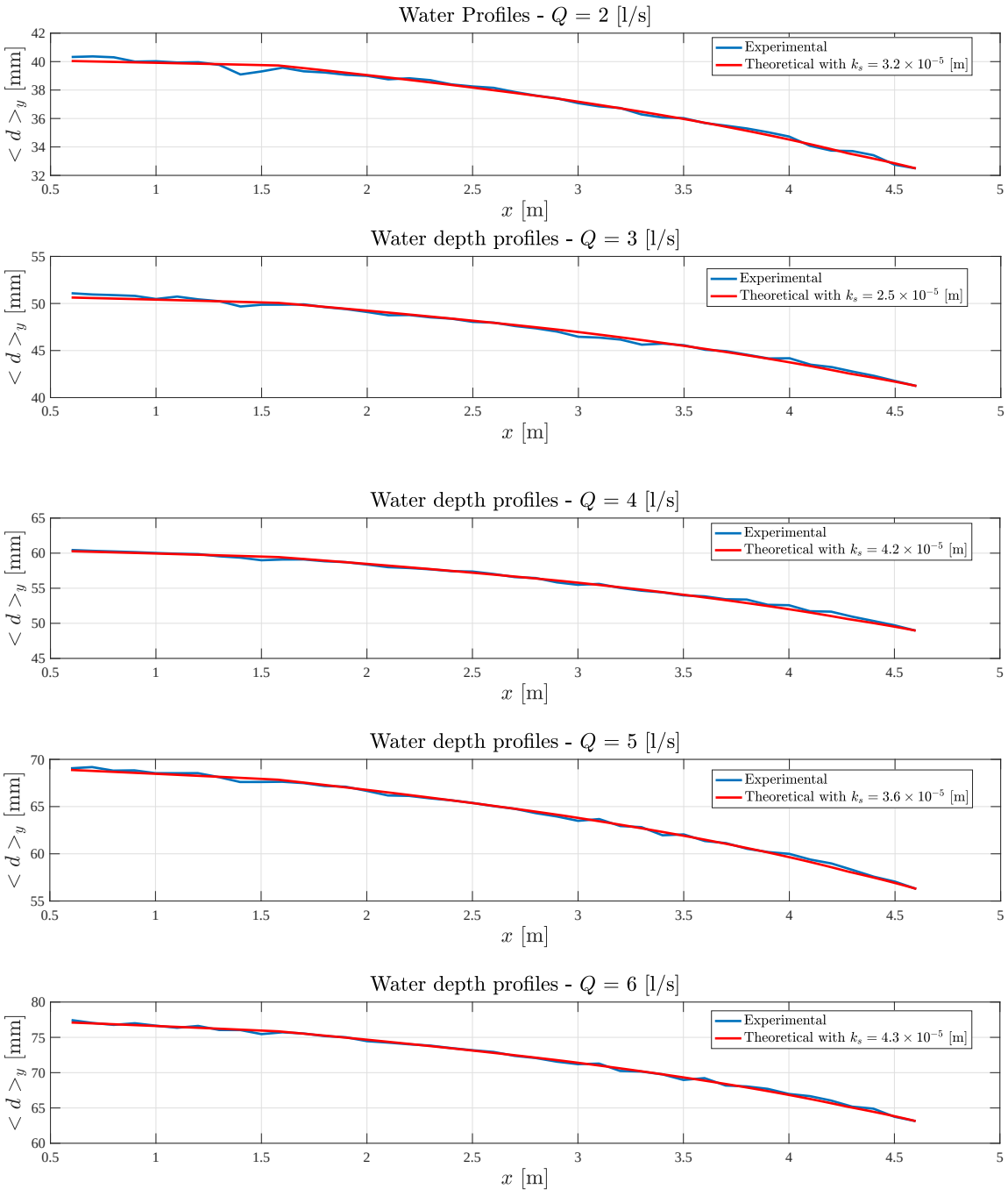

FIGURE A.4. Comparison of the water profiles, using for the theoretical profile the k_s value that generates the best fit.

A.4 Divergence tests for the US

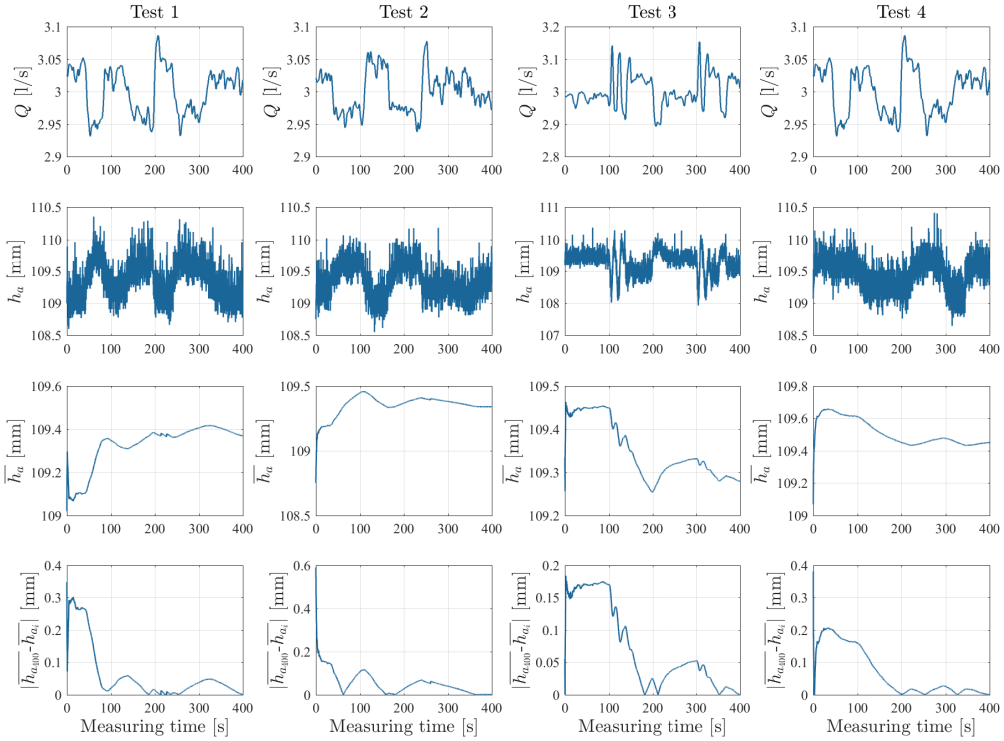

(a) $Q = 3$ l/s

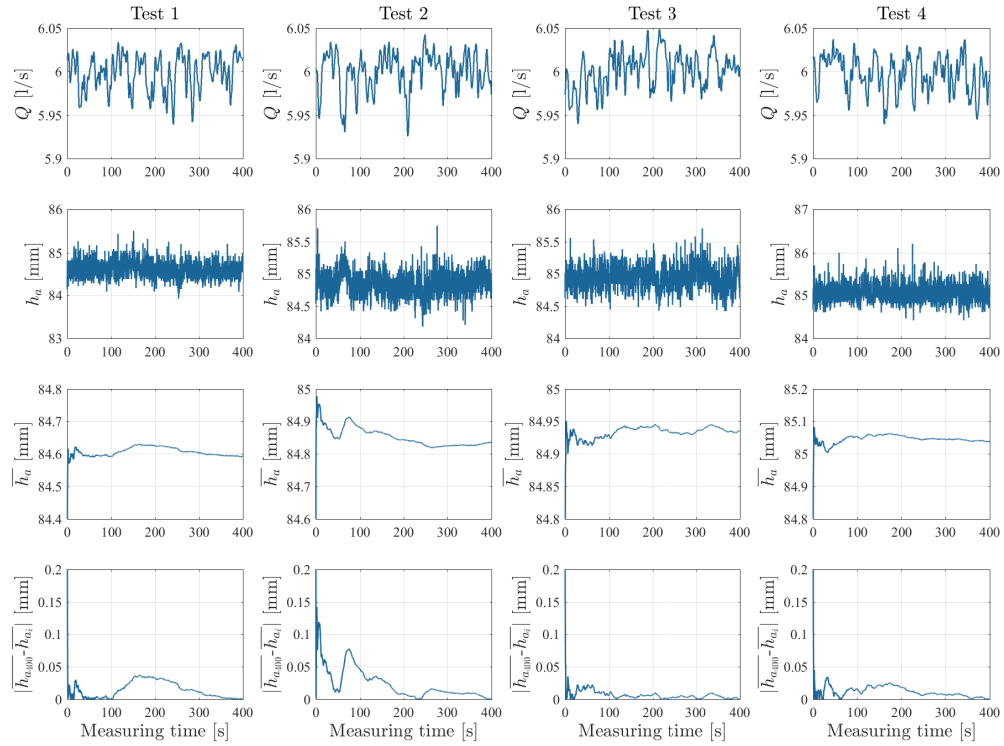

(b) $Q = 6$ l/s

FIGURE A.5. For each different flow rate, the first line shows the flow rate evolution over time, second one the instantaneous height, the third one the time-averaged height, and the final shows the difference between the total and for each instant averaged heights.

A.5 Divergence tests for the ADV

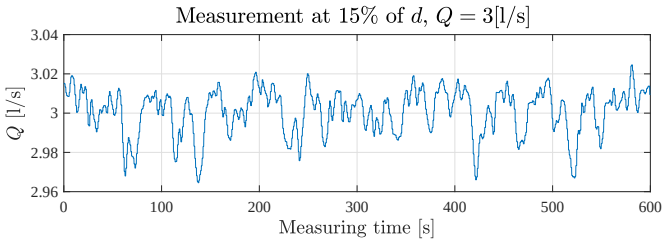

FIGURE A.6. Flow rate evolution over time during the test.

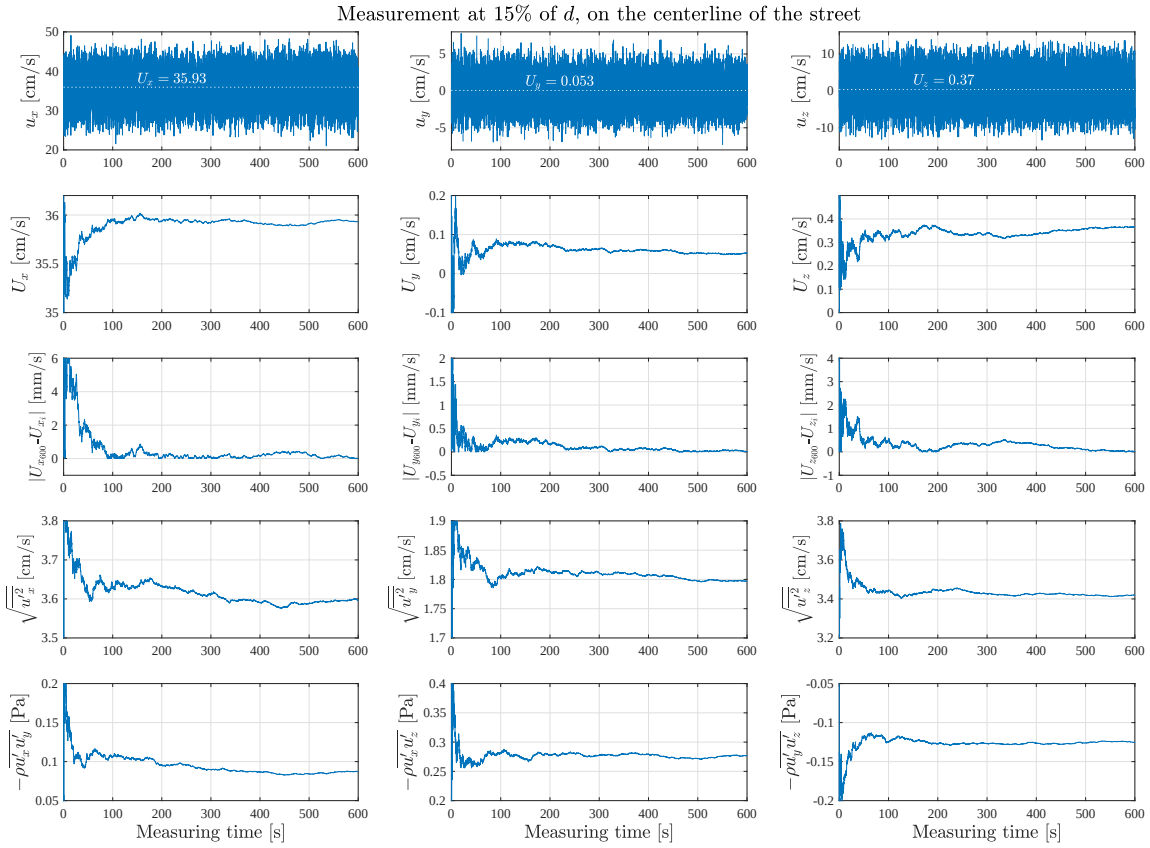

FIGURE A.7. From top to bottom, the first line of graphs shows instantaneous flow velocity, second line the time-averaged velocity, the third line shows the difference between the total and for each instant averaged velocities, the two remaining lines show turbulence parameters, the standard deviation of the set of velocity fluctuations and the Reynolds-stress respectively.

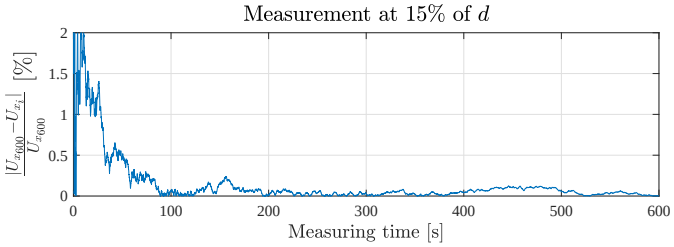

FIGURE A.8. Percentage of deviation between the final convergence value and the value at each instant.

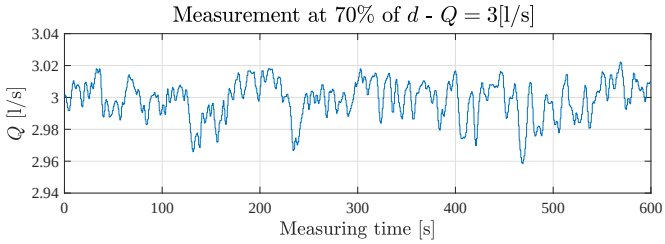

FIGURE A.9. Flow rate evolution over time during the test.

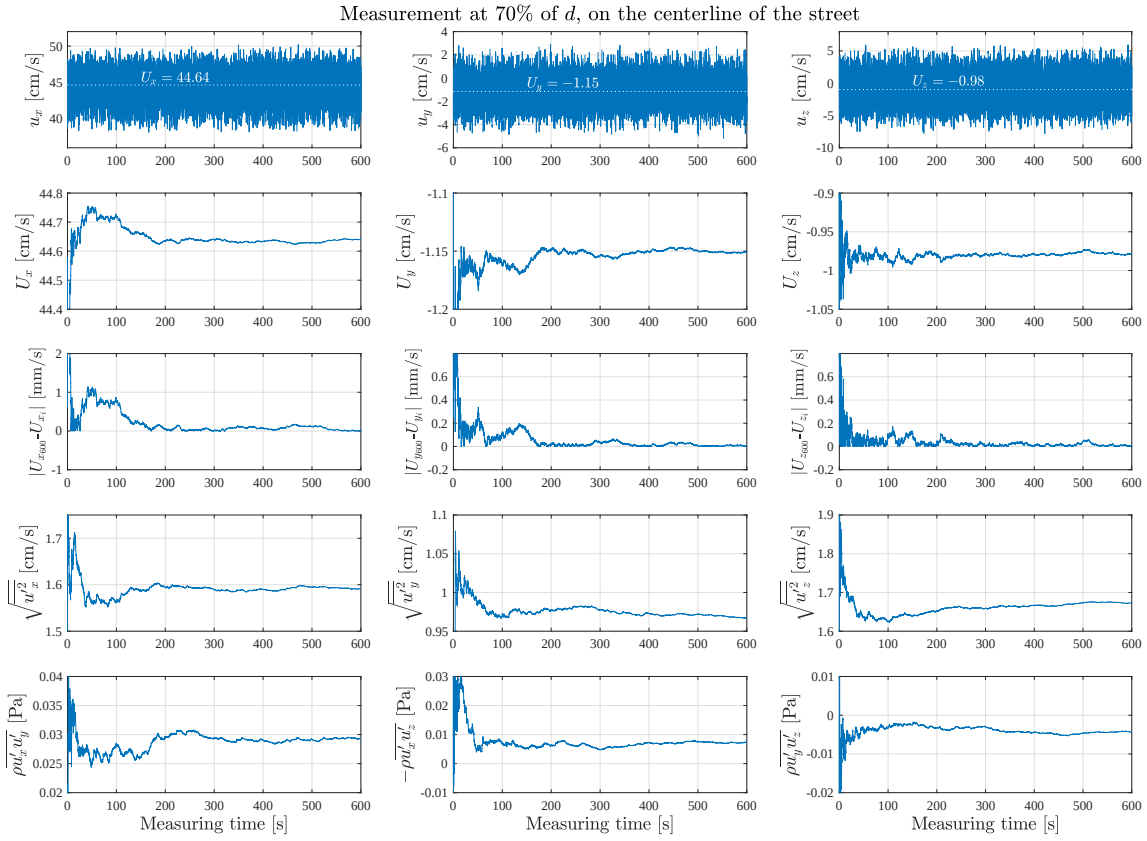

FIGURE A.10. From top to bottom, the first line of graphs shows instantaneous flow velocity, second line the time-averaged velocity, the third line shows the difference between the total and for each instant averaged velocities, the two remaining lines show turbulence parameters, the standard deviation of the set of velocity fluctuations and the Reynolds-stress respectively.

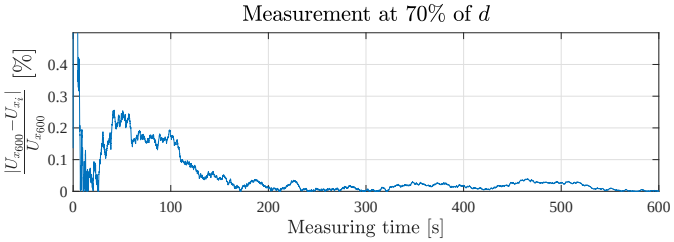

FIGURE A.11. Percentage of deviation between the final convergence value and the value at each instant.

Appendix B

Simple Street

B.1 Correction of the asymmetric flow

TABLE B.1. Different arrangements made to achieve a symmetrical flow.

Arrangement	Tank	Street
Initial	Metallic grille	Plastic grid
1	Metallic grille, plastic grid and plastic filtering material	”
2	”	Double layer of plastic grid and plastic filtering material
3	”	Four layers of misaligned plastic grid and plastic filtering material

In order to avoid rotating the ADV in each test, and due to the greater notoriety of the asymmetry on that side, the different tests to corroborate the flow symmetry in each arrangement were performed only in the left half section.

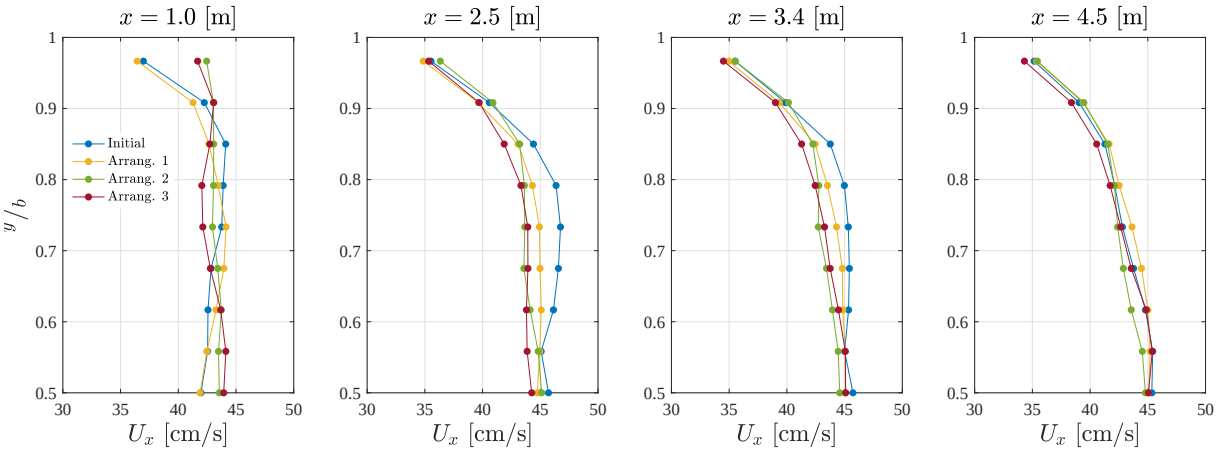

FIGURE B.1. Transverse distributions of time-averaged streamwise velocity, U_x, at 70 % of d and at various downstream x-sections (left half).

B.2 Vertical distribution of flow velocity and turbulence parameters

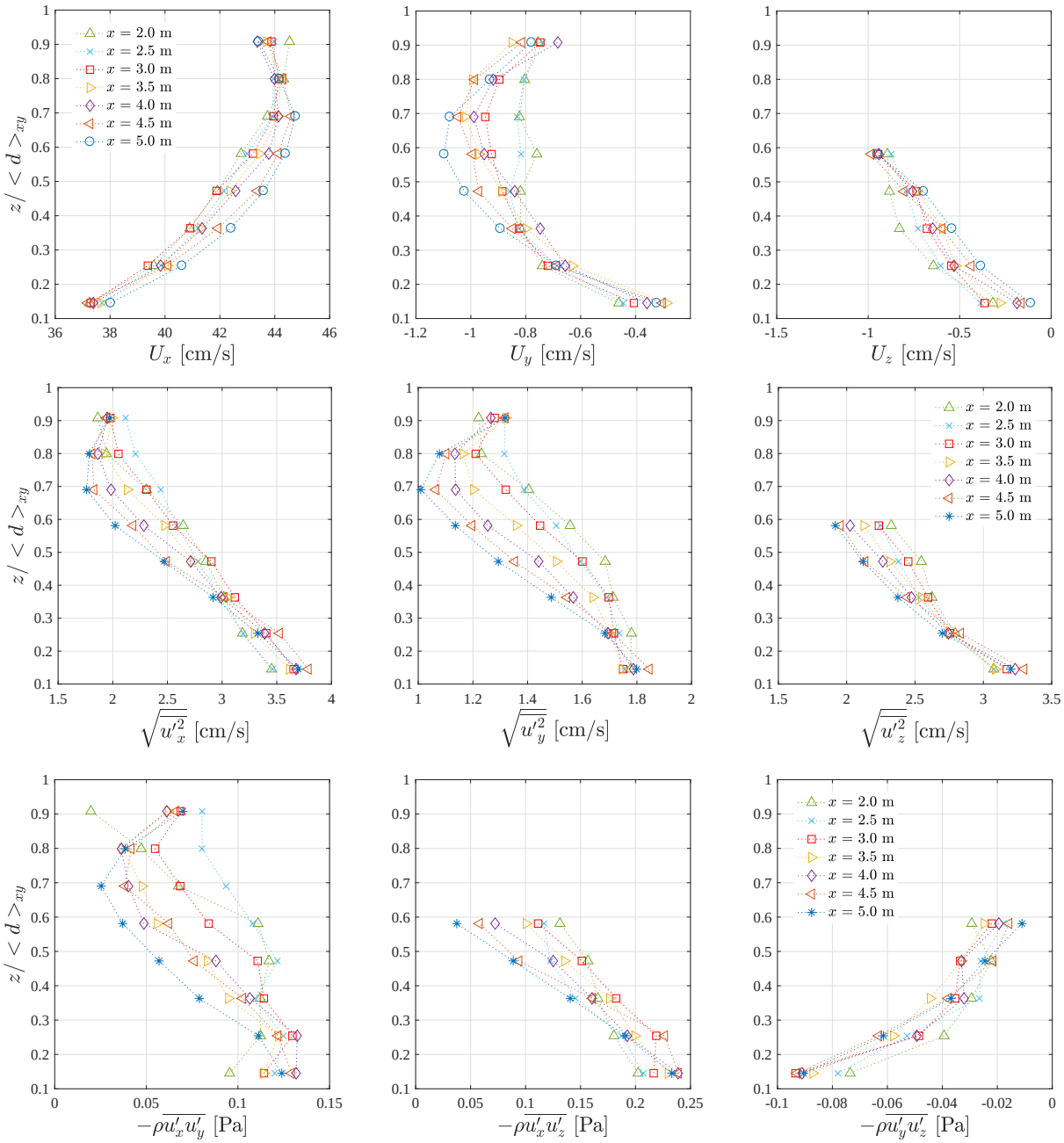

FIGURE B.2. Vertical distribution of flow velocity, flow velocity fluctuations and Reynolds-Strees for different sections on the centerline of the street, $y/b = 0.5$, (raw data).

B.3 Cross-sectional velocity distribution

The following figures show the velocity distributions before and after the flow was corrected (arrangement 3).

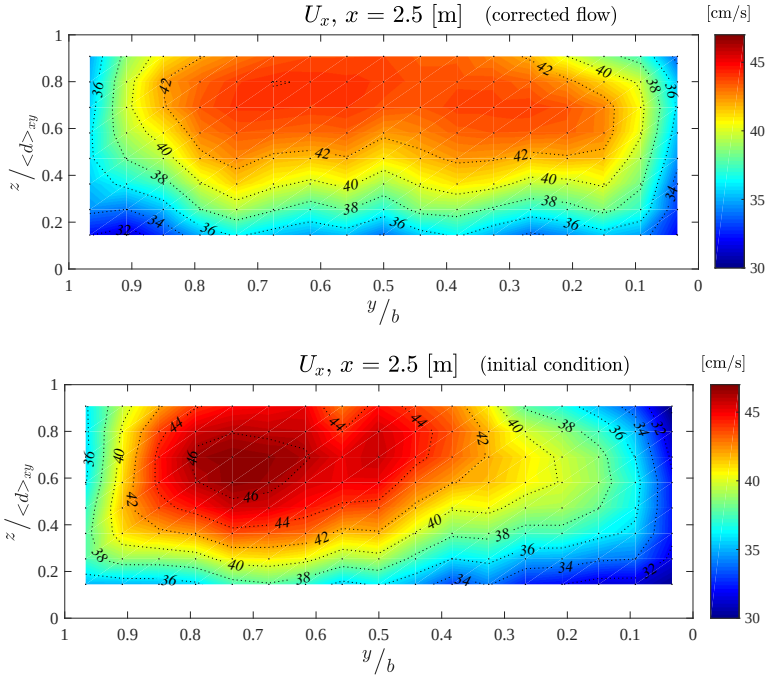

FIGURE B.3. Cross-sectional distribution of time-averaged streamwise velocity, U_x.

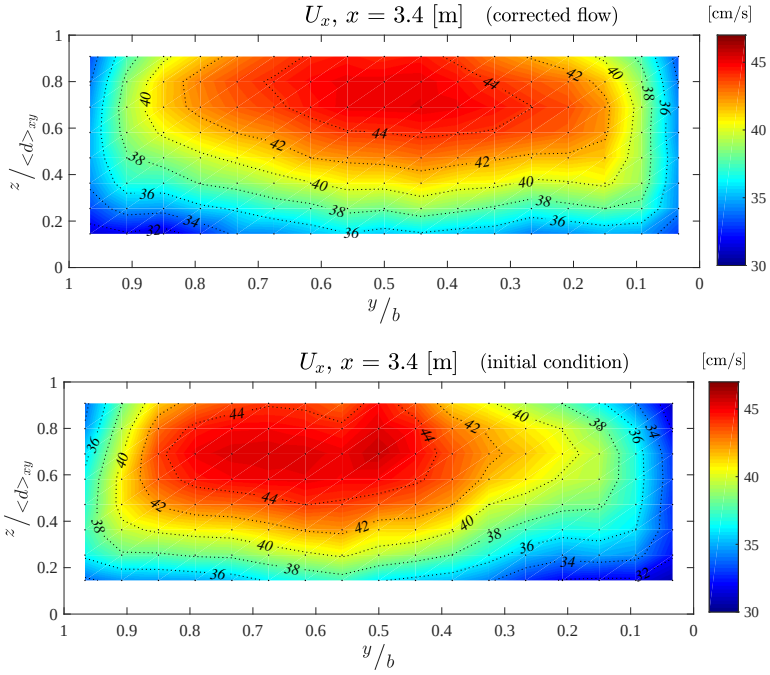

FIGURE B.4. Cross-sectional distribution of time-averaged streamwise velocity, U_x.

The following figures show the velocity fluctuation distributions in the streamwise and spanwise directions, before and after the flow was corrected.

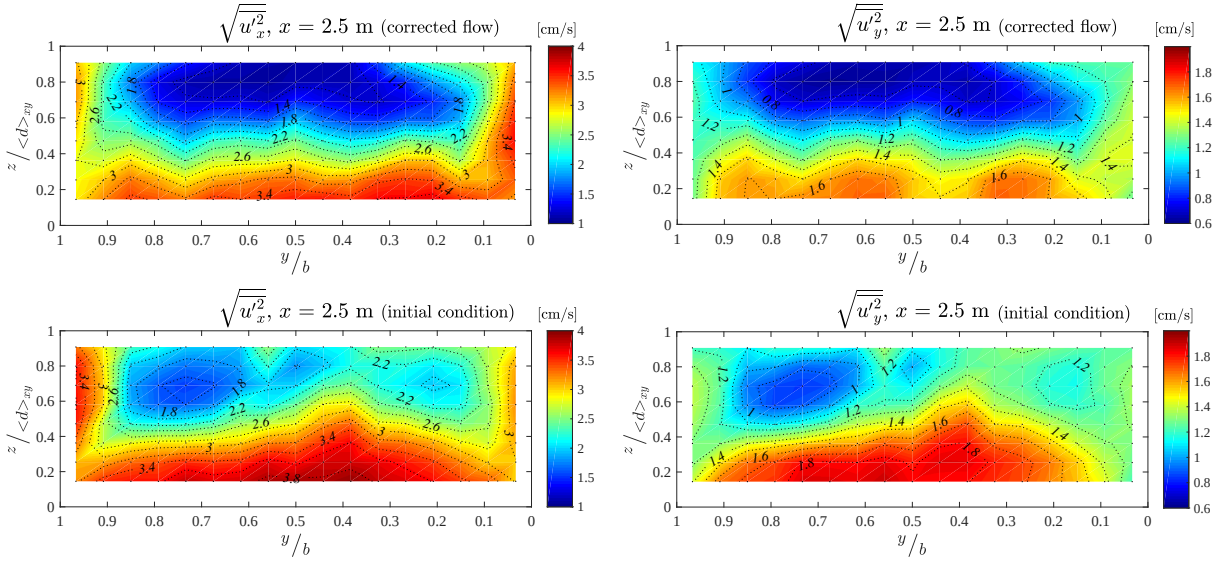

FIGURE B.5. Cross-sectional distribution of streamwise and spanwise anvelocity fluctuatios.

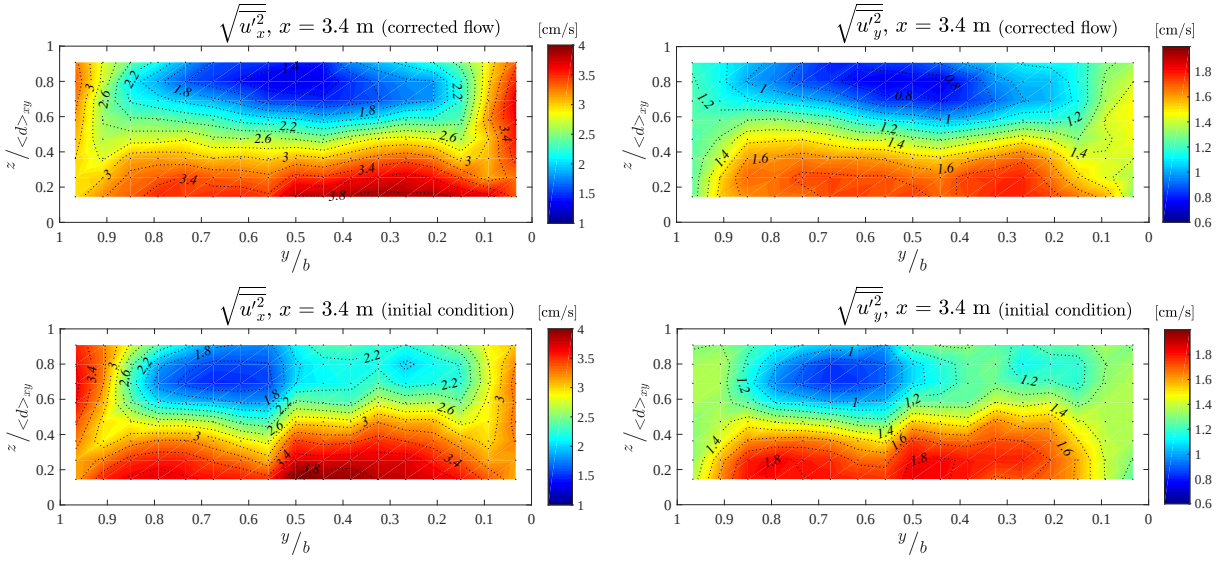

FIGURE B.6. Cross-sectional distribution of streamwise and spanwise anvelocity fluctuatios.

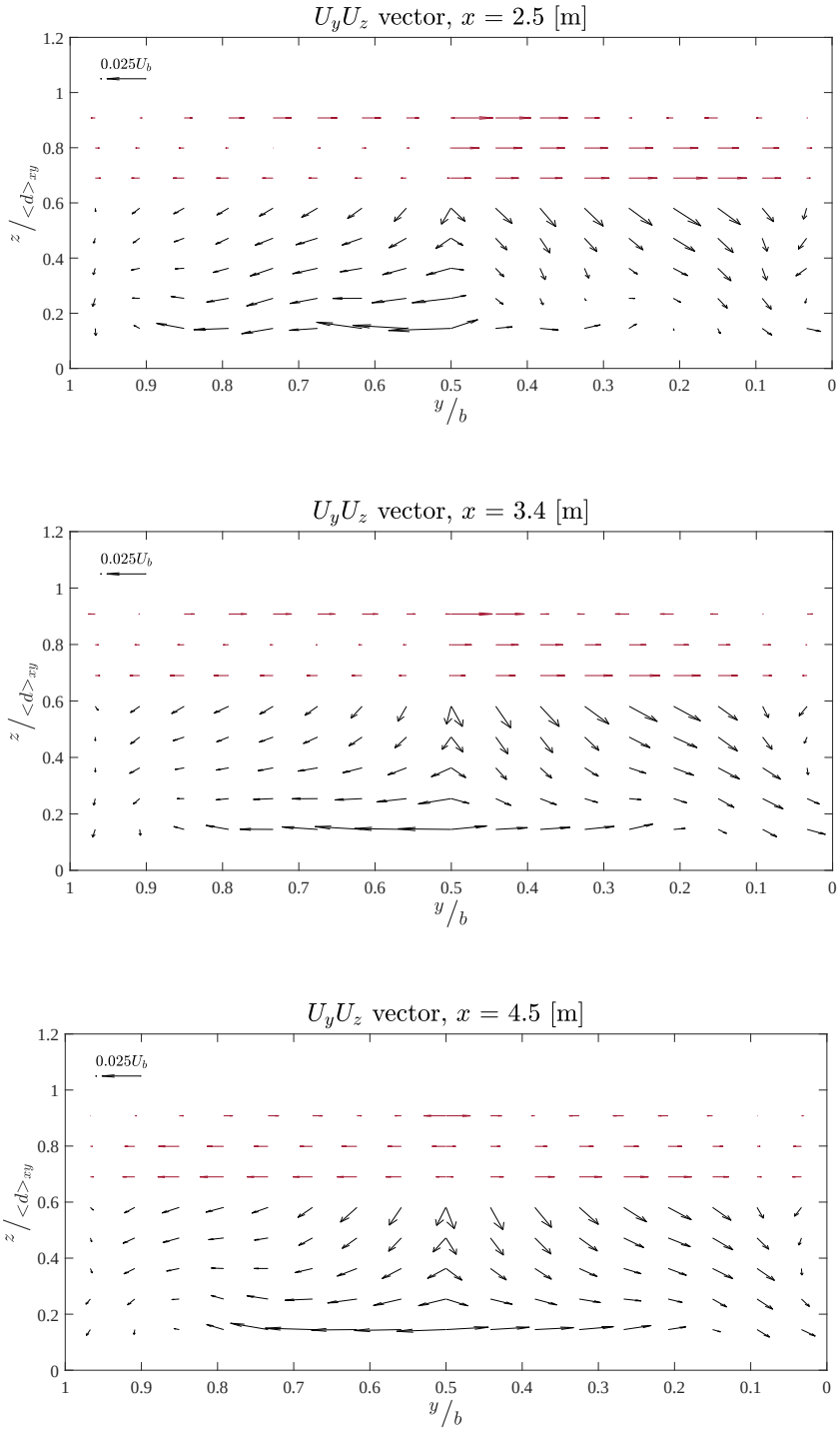

FIGURE B.7. Cross section of secondary current vectors.

Appendix C

Street with Cavities

C.1 Vertical distribution of flow velocity and turbulence parameters

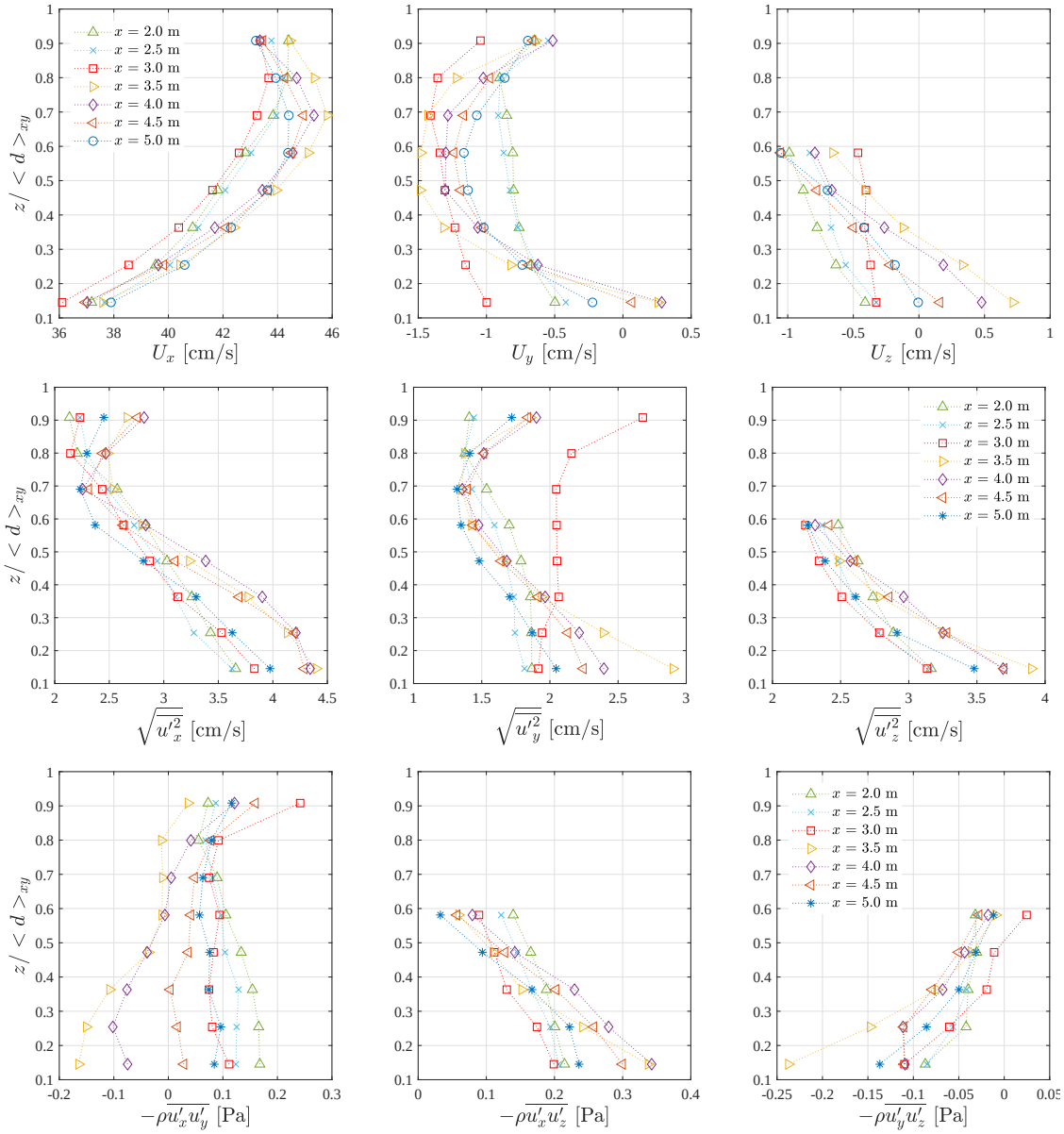

FIGURE C.1. Vertical distributions of flow velocity, flow velocity fluctuations and Reynolds-Strees for different sections on the centerline of the street (raw data).

C.2 Flow correction angles

TABLE C.1. Correction angles according to the different criteria established.

Half section		Left			Right		
x-station [m]		**2.5**	**3.4**	**4.5**	**2.5**	**3.4**	**4.5**
θ_z [°]	Criterion 1	1.70	1.59	1.76	3.52	3.87	3.57
	Criterion 2	1.41	1.30	1.37	3.93	4.22	4.12
θ_y [°]	Criterion 1	-0.16	-0.20	-0.14	-0.05	-0.88	-0.38

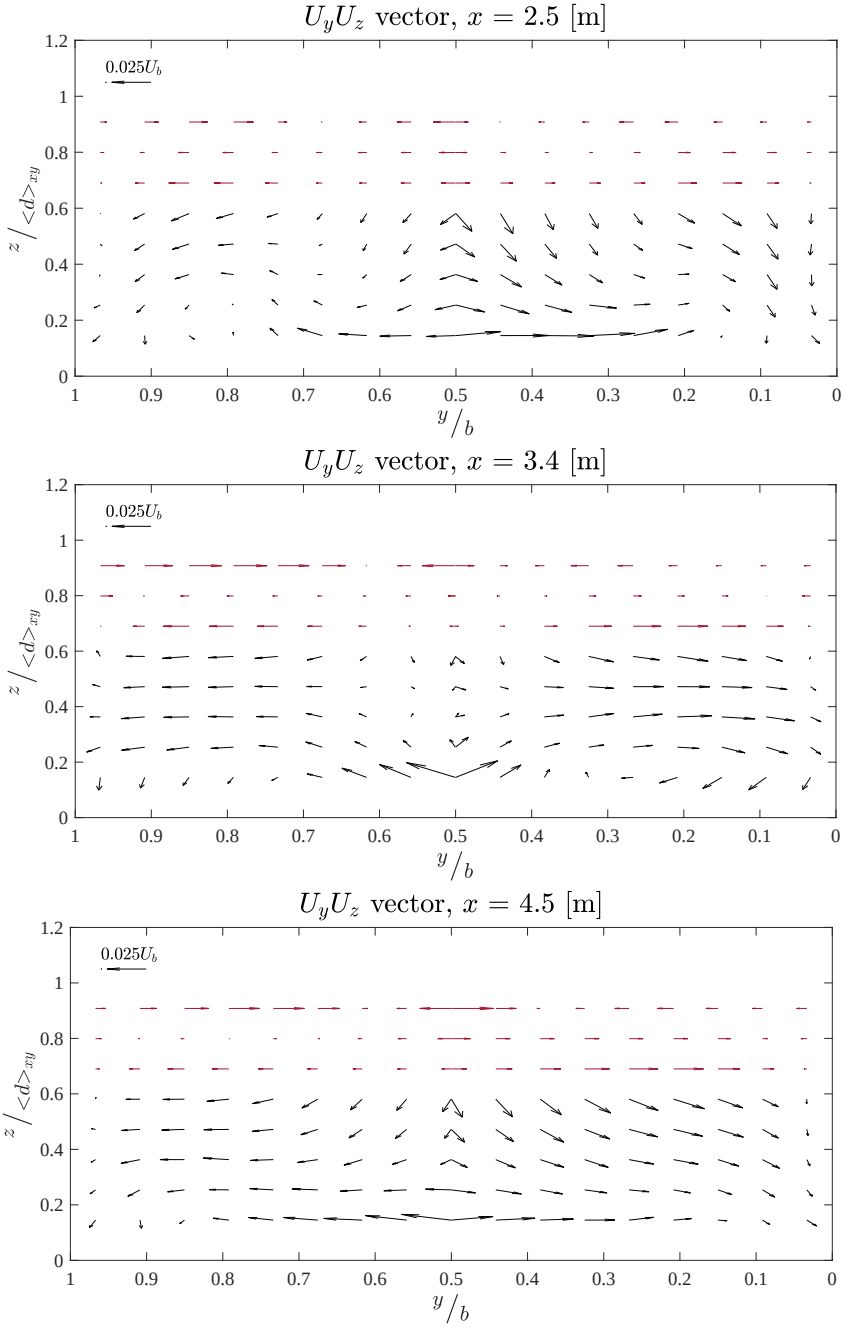

FIGURE C.2. Cross section of secondary current vectors..

Bibliography

[1] Auel, C., Albayrak, I., and Boes, R. M. (2014). *Turbulence characteristics in supercritical open channel flows: Effects of Froude number and aspect ratio.* J. Hydraul. Eng. ASCE, 140(4):04014004.

[2] Bonakdari, H., Larrarte, F., Lassabatere, L., and Joannis, C. (2008). *Turbulent velocity profile in fully-developed open channel flows.* Environmental Fluid Mechanics, 8(1), pp. 1 - 17.

[3] Cardoso, A. H., Graf, W. H., and Gust, G. (1989). *Uniform flow in a smooth open channel.* Journal of Hydraulic Research, Vol. 27 No. 5, pp. 603 - 616.

[4] Chow, V. T. (1959). *Open-channel hydraulics.* McGraw-Hill, New York.

[5] Dey, S. (2014). *Fluvial Hydrodynamics: Hydrodynamic and Sediment Transport Phenomena.* Springer-Verlag, Berlin.

[6] Dingman, S. L. (2009). *Fluvial Hydraulics.* Oxford University Press, New York.

[7] French, R. H. (1985). *Open-channel hydraulics.* McGraw-Hill, Singapure.

[8] Henderson, F. M. (1966). *Open-channel flow.* Macmillan. New York.

[9] Lalanne, C. (2017). *Rapport de Stage. Étude expérimentale d'écoulements dans un quartier de ville.* IRSTEA, France.

[10] Mignot, E., Cai, W., Launay, G., Riviere, N., and Escauriaza, C. (2016). *Coherent turbulent structures at the mixing-interface of a square open channel lateral cavity.* Physics of Fluids 28, 045104.

[11] Nezu, I., Nakagawa, H. (1993). *Turbulence in open-channel flows.* A. A. Balkema, Rotterdam.

[12] Nortek AS(2004). *VECTRINO velocimeter, user guide.* Norway.

[13] Sarkar, S. (2016). *Measurement of turbulent flow in a narrow open channel.* J. Hydrol. Hydromech., 64(3), pp. 273 - 280.

[14] Sarma, K. V. N., Lakshminarayana, P., and Lakshmana Rao, N. S. (1983). *Velocity distribution in smooth rectangular open channel.* J. Hydraul. Eng. ASCE, 109(2), pp. 270 - 289.

[15] Spretec (2016). *MAQUETTE MURI, Fourniture d'une maquette urbaine pour étudier les risques d'inondation.* Seyssins, France.

[16] Stearns, F. P. (1883). *On the current-meter, together with a reason why the maximum velocity of water flowing in open channels is below the surface.* Transactions of the ASCE, Vol. 12 No. 261, pp. 301 - 338.

[17] Yang, S., Tan, S., and Lim, S.(2004). *Velocity distribution and dip-phenomenon in smooth uniform open channel flows.* J. Hydraul. Eng. ASCE, 130(12), pp. 1179-1186.